Experimental studies of shear stress and flow separation in low Reynolds number flows

by

Matthew J. Weldon

B.S. in Mechanical Engineering, The Pennsylvania State University (2004)

Submitted to the Department of Mechanical Engineering
in partial fulfillment of the requirements for the degree of

Master of Science in Mechanical Engineering

at the

MASSACHUSETTS INSTITUTE OF TECHNOLOGY

June 2007

Author .....
Department of Mechanical Engineering
May 21, 2007

Certified by...
Thomas Peacock
Assistant Professor
Thesis Supervisor

Certified by..
Alexandra Techet
Associate Professor
Thesis Supervisor

Accepted by .....
Lallit Anand
Chairman, Committee on Graduate Students
Department of Mechanical Engineering

Experimental studies of shear stress and flow separation in low Reynolds number flows

by

Matthew J. Weldon

Submitted to the Department of Mechanical Engineering
on May 21, 2007, in partial fulfillment of the
requirements for the degree of
Master of Science in Mechanical Engineering

Abstract

Presented here is an experimental investigation of the kinematic theory of separation in unsteady two-dimensional flows, and an evaluation of a novel optical shear stress sensor. Fixed separation in the rotor-oscillator flow is studied for steady, periodic, and quasi-periodic fluid motion. Experimental results are directly compared to numerical simulations, which provide the shear-stress and pressure data required for detecting fixed separation in an unsteady flow. Good agreement between theory and experiments in determining both the location of the separation point and the angle of the separation profile is found. With the goal of directly measuring shear stress to high accuracy, an optical shear stress sensor is evaluated on a flat plate boundary layer. Wall-shear measured with the sensor is compared to that derived from particle image velocimetry (PIV) velocity profiles, and the resulting discrepancy between the two measurements is discussed.

Thesis Supervisor: Thomas Peacock
Title: Assistant Professor

Thesis Supervisor: Alexandra Techet
Title: Associate Professor

Acknowledgments

I would first like to thank my advisors, Professor Tom Peacock and Professor Alex Techet. Both Tom and Alex showed a great interest in not only my research and education, but my interests outside of academia. Needless to say, without their help and supervision, this thesis would not have been possible.

In addition, I would like to thank the members of the Experimental Hydrodynamics Lab and the Nonlinear Dynamics Lab. These lab members – in particular Tadd Truscott, Brenden Epps, Melissa Read, Paula Echeverri, Mani Mathur, and Amit Surana (though Amit is not a member of either of these labs) – were always willing to lend a hand with an experiment or share their knowledge about a particular subject or lab instrument.

I would like to thank Moneer Helu individually for his contribution to this thesis. Many of the results presented here are a direct result of Moneer's hard work.

And finally, I would like to thank all of my friends at MIT. You guys made this a great two years!

Contents

List of Figures

List of Tables

Chapter 1

Introduction

Flow separation is an important parameter in aerodynamic and hydrodynamic technology, with the location of separation having dramatic effects on the performance of a wide range of applications. Being able to identify and track the point of flow separation on, for instance, a maneuvering airplane wing has the potential to lead to increased flight performance. In addition, reduced drag, increased lift, and higher efficiencies can be realized through a knowledge of the time-resolved separation location. However, to date no experimentally proven technique exists for identifying flow separation in unsteady flows.

1.1 Background

Prandtl [9] initiated the notion that in steady two-dimensional flow, laminar boundary-layer separation occurs at the point of zero skin-friction and negative skin-friction gradient on a no-slip boundary. At this point on the boundary "a fluid-sheet projects itself into the free flow and effects a complete alteration of the motion". If we define the x-axis to be tangent to a no-slip boundary, and y-axis normal to the boundary, then boundary layer separation occurs at the point $\mathbf{p}(x, y) = (\gamma, 0)$ where

$$\tau_w(\gamma) = 0, \qquad \tau_{w,x}(\gamma) < 0 \tag{1.1}$$

where $\tau_w(x) = \mu\frac{\partial u}{\partial y}(x,0)$ is the skin-friction, (u,v) is the two-dimensional velocity field, and μ is the dynamic viscosity.

More generally, the criterion from equation 1.1 can be applied to separation on any scale in a laminar, two-dimensional, steady flow. Examples other than boundary-layer separation include: separating streamlines in Stokes flows, such as Moffatt corner-eddies [8] and the rotor-oscillator flow [4]; and small-scale separation structures within the boundary layer, such as a separation bubble [13]. In all cases, the angle of separation with respect to the boundary, α, can be determined from a knowledge of the skin-friction gradient $\tau_{w,x}$, and pressure gradient p_x, and is given by [6]:

$$\tan(\alpha) = \frac{-3\tau_{w,x}(\gamma)}{p_x(\gamma,0)} \tag{1.2}$$

For an unsteady, laminar, two-dimensional flow, the zero-skin-friction principle is not necessarily a reliable indicator of flow separation [10, 3]. Indeed, in an unsteady flow one must be very careful to define what is meant by "separation". We herein follow the lead of Prandtl and use it to mean the sudden ejection of fluid from the vicinity of a rigid boundary. At present an experimentally proven criteria for identifying unsteady separation does not exist.

Sears & Telionis [10] proposed the Moor-Rott-Sears (MRS) criterion, which states that in a frame of reference moving with the separating structure, unsteady separation occurs at a point off the boundary where both the velocity and the shear instantaneously vanish. For truly unsteady flows, however, these instantaneous quantities are not reliable indicators; to determine material transport away from a boundary one must consider the time integrated effect of an unsteady flow. Van Dommelen & Shen [12] adopted a Lagrangian approach which identified separation with the appearance of a sharp material spike associated with the formation of a singularity in the Lagrangian formulation of the boundary layer equations. It has since been noted, however, that a singularity in the boundary layer equations is not a necessary condition for separation [7]. A Lagrangian definition of fixed separation in unsteady flows was later proposed by Shariff, Pulliam, & Ottino [11], and Yuster & Hackborn

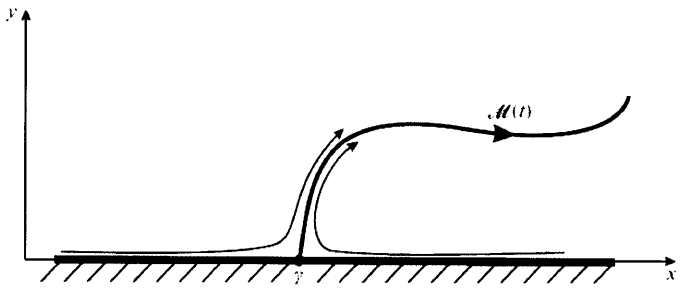

Figure 1-1: A time-dependent unstable manifold $\mathcal{M}(t)$ originating from the fixed separation point $\mathbf{p} = (\gamma, 0)$ on a no-slip boundary. Figure taken from [3]

[14] made the approach mathematically rigorous for near-steady time-periodic incompressible flows. Building on this, Haller [3] developed a kinematic theory of unsteady separation for two-dimensional compressible flows with arbitrary time dependence.

1.2 Kinematic theory of unsteady separation

1.2.1 General incompressible unsteady flow

Here we briefly summarize the dynamical systems approach to fixed separation in two-dimensional, unsteady flows [3]. The separation profile is a distinguished, time-dependent material line, or unstable manifold, that originates from a fixed point, the separation point, on the no-slip boundary (figure 1-1). In an incompressible flow any *fixed* separation point $\mathbf{p} = (\gamma, 0)$, at time t_0, satisfies:

$$\int_{-\infty}^{t_0} \tau_w(\gamma, t)\ dt = 0, \qquad \int_{-\infty}^{t_0} \tau_{w,x}(\gamma, t)\ dt < 0 \tag{1.3}$$

That is to say, the fixed separation point occurs at the location where the time average of the skin-friction is zero and the time average of the skin-friction gradient is negative.

The first condition in equation 1.3 is the necessary condition for the existence of a separating or re-attaching material line at $\mathbf{p}$. The second condition distinguishes $\mathbf{p}$ from a re-attachment point, ensuring material ejection from $\mathbf{p}$ into the mean flow. This condition is also intimately related to the strength of separation, and has the

potential to be used to distinguish between small scale separation and boundary-layer separation. For steady incompressible flows, equation 1.3 further simplifies to the original Prandtl criterion in equation 1.1.

The time-dependent orientation of an unstable manifold (separation profile), along which fluid particles are ejected from the wall, can be calculated from distributed skin-friction and wall-pressure measurements. Specifically, the separation angle at time t_0 is found by:

$$\tan\alpha(t_0) = \frac{-3\int_{t_0}^{-\infty} \tau_{w,x}(\gamma,t)\ dt}{\int_{t_0}^{-\infty}\left[p_x(\gamma,0,t) + 3\tau_{w,x}(\gamma,t)\int_{t_0}^{t}(1/\mu)\tau_w(\gamma,t)ds\right]\ dt} \tag{1.4}$$

where μ is the dynamic viscosity of the fluid. In the limit of a steady flow this reduces to (1.2). Additional formulae for the curvature of the separation profile, as well as higher order expressions, were also derived. Moreover, (1.3) and (1.4) can be generalized to any compressible mass-conserving fluid flow.

1.2.2 Periodic incompressible flow

For periodic flow of period T, the fixed separation criteria in (1.3) simplifies to:

$$\int_0^T \tau_w(\gamma,t)\ dt = 0, \qquad \int_0^T \tau_{w,x}(\gamma,t)\ dt < 0 \tag{1.5}$$

In this case, only one period of skin-friction knowledge is required for the calculation of the separation location to be exact, greatly reducing the amount of time-history required to converge to a fixed separation point. Likewise, the periodic orientation of the unsteady separation profile simplifies to:

$$\tan\alpha(0) = \frac{-3\int_0^T \tau_{w,x}(\gamma,t)\ dt}{\int_0^T\left[p_x(\gamma,0,t) + 3\tau_{w,x}(\gamma,t)\int_0^t(1/\mu)\tau_w(\gamma,t)ds\right]\ dt} \tag{1.6}$$

Again, only one period of skin-friction and wall-pressure gradient is needed for an exact calculation of the periodic unsteady separation angle.

1.3 Preview of chapters

For an experimental implementation of the kinematic theory of unsteady separation skin-friction and pressure gradients at the wall must be known. As such, a novel optical skin friction sensor is discussed in chapter 2. Experimental techniques used to evaluate the sensor on a flat plate boundary layer are presented in chapter 3, and results are discussed in chapter 4.

The kinematic theory of unsteady separation was then studied experimentally and numerically in the low Reynolds number rotor-oscillator flow, and the experimental apparatus and methods are given in chapter 5. Chapter 6 presents results of the study, and a final conclusion is provided in chapter 7.

Chapter 2

Optical shear stress sensor

To predict the location and shape of a separating material spike experimentally from engineering quantities using equation 1.3 and equation 1.4, the shear stress and pressure gradients at the boundary must be measured. Shear stress, in particular, is a difficult measurement to obtain. Typical experimental methods for measuring shear stress include hot wire and hot film sensors, surface mounted MEMS force-balance sensors, and oil film interferometry [1]. Each of these techniques is not without its drawbacks, however. Hot wire and hot film sensors require calibration to obtain accurate results, and can suffer from sensor drift. Surface mounted force balances result in a spatial averaging of the shear stress over the area of the sensor surface, and have poor high-frequency response. Oil film interferometry requires specific surface and lighting requirements, and is only practical in a controlled laboratory setup.

A recent development in shear sensor technology is the optical "MicroS Shear Stress Sensor", produced by Measurement Science Enterprises (MSE). The sensor body is shown in figure 2-1, and figure 2-2 provides a close look at the optical surface of the sensor. The MicroS sensor uses optical techniques to measure the time of flight of particles within the linear region of the boundary layer (the laminar sublayer in turbulent boundary layers). From these measurements, the wall shear stress can be derived, as shown below. The advantages to such a sensor include a non-invasive measurement technique, high spatial resolution (with a translating sensor, or array of sensors), and a calibration-free measurement.

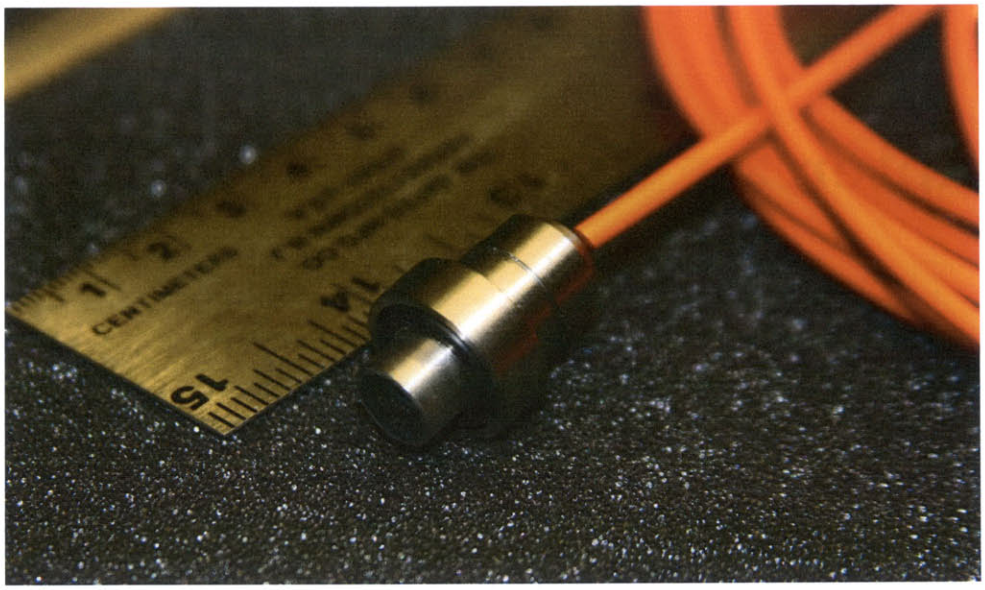

Figure 2-1: Shear stress sensor

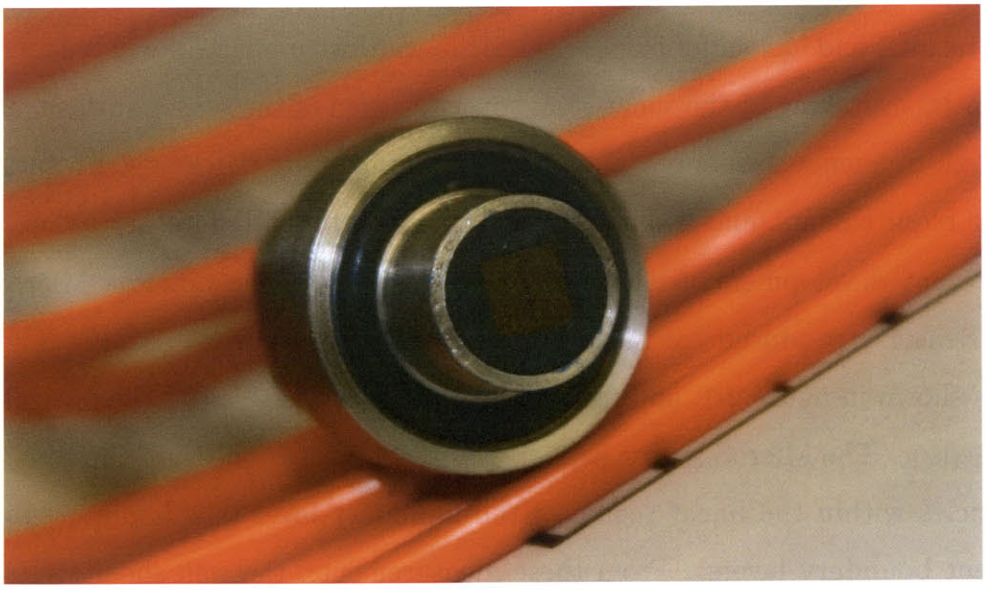

Figure 2-2: Shear stress sensor optical surface

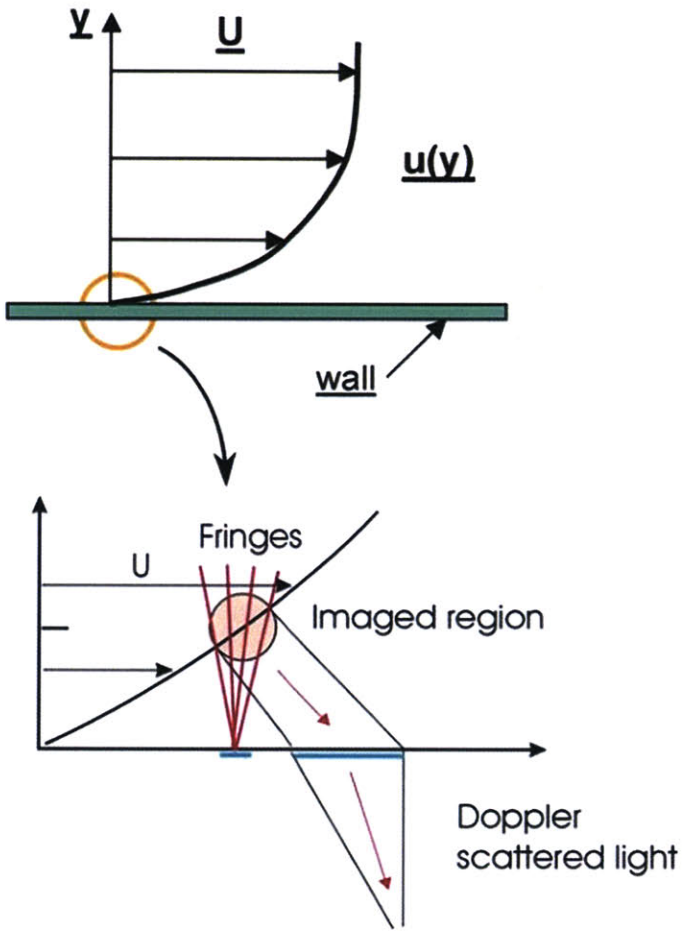

Figure 2-3: Sketch of shear stress sensor. Figure taken from [1]

The optical shear sensor emits a series of diverging laser fringes, having a rate of divergence k, and an origin located on the sensor surface. As a particle suspended in the fluid travels through the diverging fringes at some distance y away from the wall, light is scattered at a frequency f proportional to the speed of the particle $u(y)$ and the spacing of the fringes $\delta(y)$ according to:

$$u(y) = f \cdot \delta(y) = f \cdot k \cdot y \tag{2.1}$$

The light scattered by a passing particle is picked up with an optical sensor, which is located on the surface of the sensor and focused on a volume of fluid a small distance from the wall. A schematic of the sensor configuration is presented in figure 2-3. The optical sensor output is filtered and analyzed with a software package provided with the sensor to extract the frequency of the scattered light.

The distance of the measurement volume from the wall is chosen such that the measurement volume is well within the linear region of the boundary layer. This linear region is the part of the boundary layer nearest the wall where the velocity of the fluid, $u(y)$, increases with increasing distance from the wall, y, at a near constant rate, resulting in a linear velocity profile. This profile is further discussed in chapter 3.

The slope of the velocity profile at the wall is proportional to the wall shear stress τ_w given the relation:

$$\tau_w = \mu \left. \frac{\partial u}{\partial y} \right|_w \tag{2.2}$$

where μ is the dynamic viscosity of the fluid. Using the assumption of a linear velocity profile discussed above, the shear stress can be calculated as

$$\tau_w = \mu \frac{u(y) - u(0)}{y} \tag{2.3}$$

Invoking the no-slip condition at the boundary, $u(0) = 0$, the shear stress becomes:

$$\tau_w = \mu \frac{u(y)}{y} = \mu \frac{f \cdot k \cdot y}{y} \tag{2.4}$$

which simplifies to the relation:

$$\tau_w = \mu \cdot f \cdot k \tag{2.5}$$

The shear stress, then, depends only on the viscosity of the fluid, the divergence rate of the laser fringes, and the frequency of the scattered light, with no calibration necessary.

Chapter 3

Optical shear stress sensor evaluation – experimental methods

To evaluate the performance of the Measurement Science Enterprises (MSE) optical shear sensor in a low speed flow, such as the flow encountered in a low Reynolds number separation experiment, a simple benchmark wall-shear test was needed. As such, a flat plate boundary layer experiment was created in a low speed water channel, and the wall-shear was calculated both from the shear sensor output and from calculations based on particle image velocimety (PIV) velocity profiles. Wall-shear was studied rather than wall shear stress for simplicity, as the two quantities are related by equation 2.2. This chapter describes the experimental apparatus and methods employed, while chapter 4 discusses the results of the experiments.

3.1 Water channel

A low speed, open top water channel was used to drive flow past the flat plate model in the experiments. The water channel, shown in figure 3-1, was constructed to have a settling tank and converging region upstream of the test section, an acrylic, open top test section of dimensions 15.5 cm wide, 30.5 cm tall, and 62.0 cm long, and a downstream settling tank. Flow was drawn by a centrifugal pump from the bottom of the downstream settling tank and pumped to the upstream settling tank through

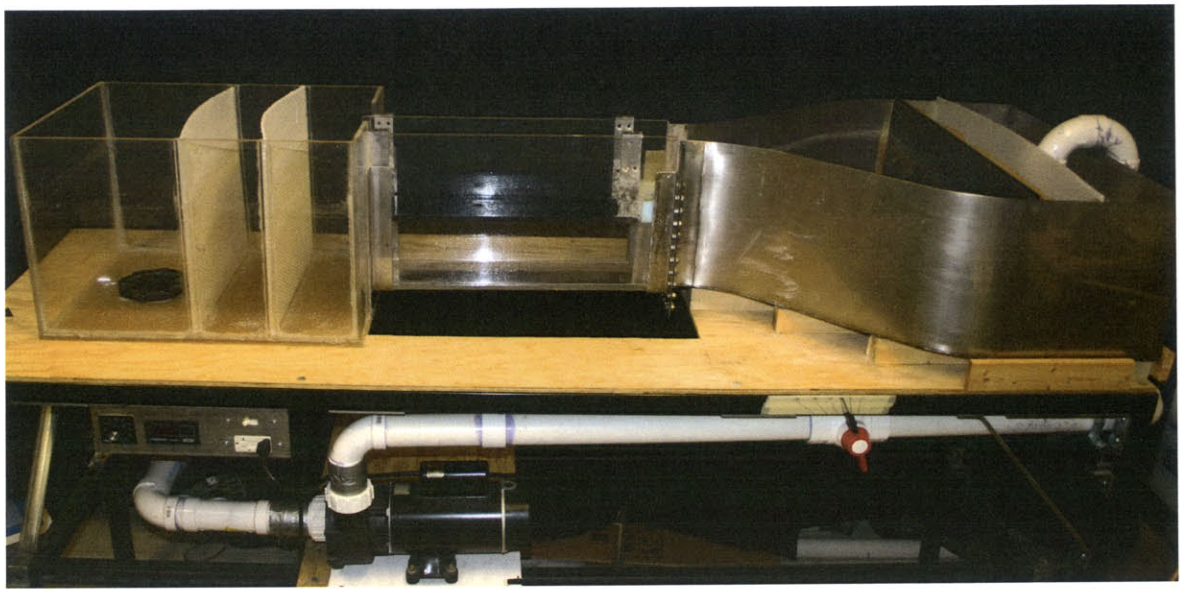

Figure 3-1: Experimental water channel

3-inch PVC tubing. A ball valve was installed in the tubing downstream of the pump, and the flow was returned to the upstream settling tank through a perforated section of 3-inch tube that spanned the width of the settling tank. This section of tube was wrapped in a porous plastic mesh to ensure that low-speed, uniform flow was discharged from the tubing.

The flow was conditioned leading into the test section by placing a honeycomb plastic sheet and a sheet of porous plastic mesh in the upstream settling chamber. These two sheets of material created more uniform flow leaving the settling chamber, and damped out higher amplitude fluctuations. In addition, a flow straightener was placed at the start of the test section, consisting of an array of parallel, 7 cm long, thin walled plastic tubes having a diameter of 5 mm; and a fine wire screen was placed 2 cm downstream of the flow straightener. Two more sheets of plastic honeycomb were placed in the downstream settling chamber to damp fluctuations in this chamber as well. The result of the aforementioned flow conditioning was flow nearly devoid of large three-dimensional fluctuations in the center of the test section, as visualized by injecting dye into the fluid at the start of the test section.

Flow velocity in the test section was controlled with both a ball valve located in the tubing leading from the pump and a variable rheostat connected to the pump

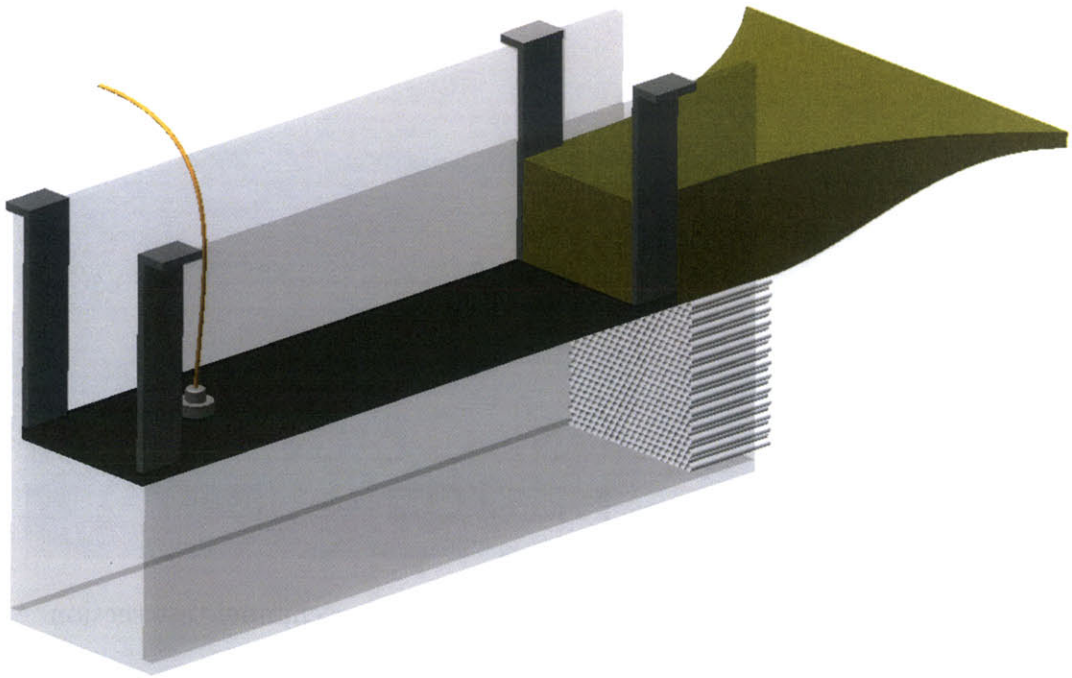

Figure 3-2: Flat plate water channel model

power supply. Coarse flow adjustments were made by opening or closing the ball valve, while fine adjustments were made by varying the voltage supplied to the electric pump motor with the rheostat.

3.2 Flat plate model

A flat plate model was installed in the test section of the water channel as the experimental model. A schematic of the complete model is shown in figure 3-2, and figure 3-3 shows a picture of the installed model. The flat plate comprised a piece of sheet acrylic, spanning the length and width of the test section, and mounted 13.5 cm from the floor of the test section. The bottom-facing surface of the flat plate was used as the experimental surface of interest. A converging boundary at the top of the water channel, leading to the test section, was created from rigid closed-cell foam. The combination of the upper converging boundary and the top-mounted flat plate resulted in a closed test section. A boundary layer was allowed to grow on the flat plate, and the shear sensor was flush-mounted with the lower surface of the flat

Figure 3-3: Flat plate model installed in water channel test section

plate 31.0 cm downstream of the final flow conditioning screen. The acrylic sheet was painted flat black, then sanded smooth, to reduce reflections of the laser illumination while collecting PIV data.

3.3 Shear sensor

The shear sensor, flush mounted on the flat plate, was aligned with the flow direction. The flow was seeded with silicone carbide particles, having a nominal diameter of 1.5 μm, and a density of 3.2 g/cc. While the density of these particles is significantly greater than that of water, the small diameter ensured that the settling velocity of the particles in water was much slower than the fluid velocity in the test section. It can be assumed that the particles follow the flow to a high degree of accuracy.

The shear sensor tested had a fringe divergence rate of $k = 0.0572$, and the measurement region was centered approximately 140 μm from the sensor surface. The output from the shear sensor was input to a Krohn-Hite Butterworth filter rather than the standard MSE-supplied band-pass filter to allow greater control of the signal filtering. The filter was configured as a bandpass filter, with the low-frequency and high-frequency cutoff values experimentally determined for each flow velocity such

that high- and low-frequency noise was eliminated, yet the desired signal was not attenuated. The filter also applied a 30 dB gain to the input signal. The filter output was acquired by a National Instruments PCI-5112 high speed digitizer and processed with the MSE acquisition software. Within the MSE processing software, the trigger value for collecting samples was set to 0.3 V. Each triggered sample was then validated by the software by discarding any sample below a minimum, user defined, signal-to-noise ratio (SNR). Minimum SNR values ranging from 1 dB to 15 dB were studied.

The wall-shear $(\partial u/\partial y)|_w$ for each free stream velocity was calculated as the mean of the shear samples:

$$\left.\frac{\partial u}{\partial y}\right|_w = \frac{1}{N}\sum_{i=1}^{N}\left.\frac{\partial u}{\partial y}\right|_{w,i} = \frac{1}{N}\sum_{i=1}^{N} f_i \cdot k \tag{3.1}$$

where N is the number of validated samples. Our confidence in the accuracy of the mean calculation can be expressed by the standard deviation of the mean ($SDOM$), based on the number of acquired samples and the standard deviation of the sample set $\sigma_{(\partial u/\partial y)|_w}$. The $SDOM$ is defined as:

$$\sigma_{\frac{\partial u}{\partial y}|_w} = \frac{\sigma_{\frac{\partial u}{\partial y}|_w}}{\sqrt{N}} \tag{3.2}$$

The experimental uncertainty in the mean wall-shear value due to scatter in the data can therefore be reduced by taking a very large number of sample points.

3.4 Particle image velocimetry (PIV)

Velocity profiles at the sensor location were obtained with a PIV system. For the PIV profiles, the flow was seeded with hollow glass spheres, having a nominal diameter of 8-12 μm, and a density of 1.05-1.15 g/cc. Illumination was provided in the form of a light sheet aligned parallel to the flow direction, with a frequency-doubled Nd:YAG laser emitting light at a 532nm wavelength. Images were acquired from the side of the

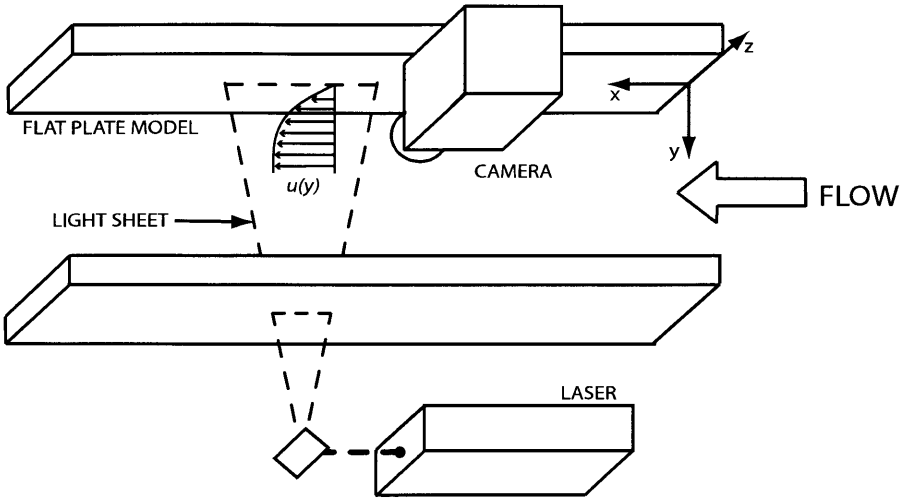

Figure 3-4: PIV experimental setup

test section with a Megaplus ES 4.0 camera fitted with a Nikon 105mm macro lens and a 532nm band-pass lens filter. The lens, at its minimum focal distance, resulted in an image size of 1.64 cm x 1.64 cm at a full resolution of 2048 x 2048 pixels. A schematic of the PIV arrangement is given in figure 3-4. The images were processed with LaVision DaVis PIV software, using a processing window size of 16 x 16 pixels. The combination of a very small image size and a small processing window size allowed many vectors to be calculated inside the boundary layer. The mean velocity profiles were taken as the ensemble average of 120 instantaneous velocity profiles.

The wall-shear was derived from the velocity vectors by fitting a weighted least squares regression line to the linear region of the boundary layer velocity profile. To determine the limit of this linear region, the velocity profile was modeled by the theoretical Blasius solution for a flat plate boundary layer, shown in figure 3-5 [5]. Here, the velocity profile is plotted as the u velocity component normalized with the freestream velocity, U. The velocity growth is plotted against the similarity variable η, given as:

$$\eta = y\sqrt{\frac{U}{\nu x}} \tag{3.3}$$

where the x-axis begins at the leading edge of the flat plate and is aligned with the flow direction, the y-axis begins at the surface of the flat plate and is aligned normal to the flat plate, and ν is the kinematic viscosity of the fluid. The Blasius velocity

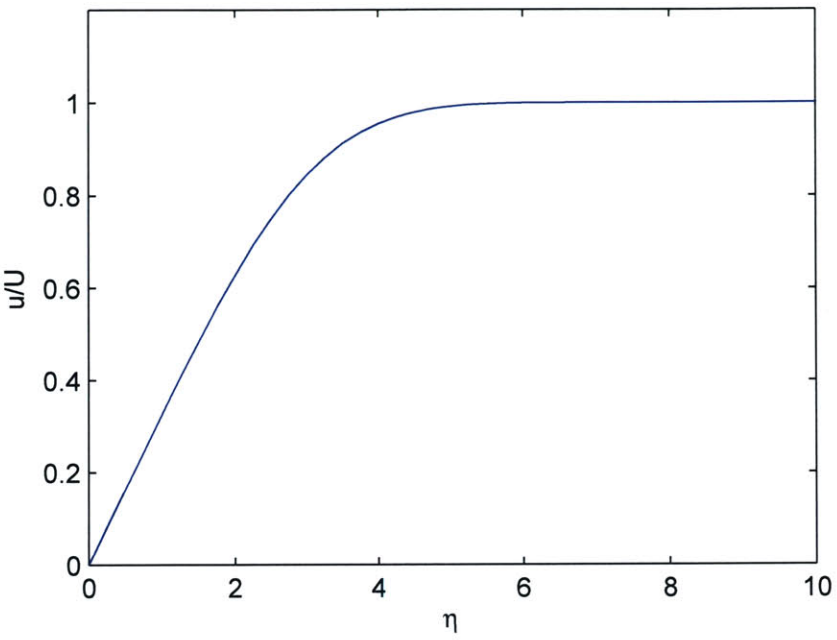

Figure 3-5: Blasius flate plate velocity profile

profile exibits a near constant slope for small values of η, then rapidly asymptotes to the free stream velocity as η grows. For each experimental case studied here, the x-location of the sensor, freestream velocity, and kinematic viscosity of the fluid are all held constant, leaving η to scale directly with the distance from the plate, y.

The linear limit of the velocity profile for the Blasius model was taken to be the point at which the velocity calculated by the Blasius solution deviated by more than 1% from that calculated with a constant shear approximation:

$$\frac{u}{U}(\eta) = \left.\frac{d(\frac{u}{U})}{d\eta}\right|_{\eta=0} \cdot \eta \tag{3.4}$$

This linear limit was found to be the point where $u/U = 0.3746$, as shown in figure 3-6. Alternatively, the linear limit can be defined at a value of η; however, u/U can be determined experimentally to a higher accuracy than η. Although the velocity profile observed in the experiments did not exactly match the Blasius profile, this cutoff value provides a very good approximation for the point where our velocity profiles ceased to exhibit a linear trend.

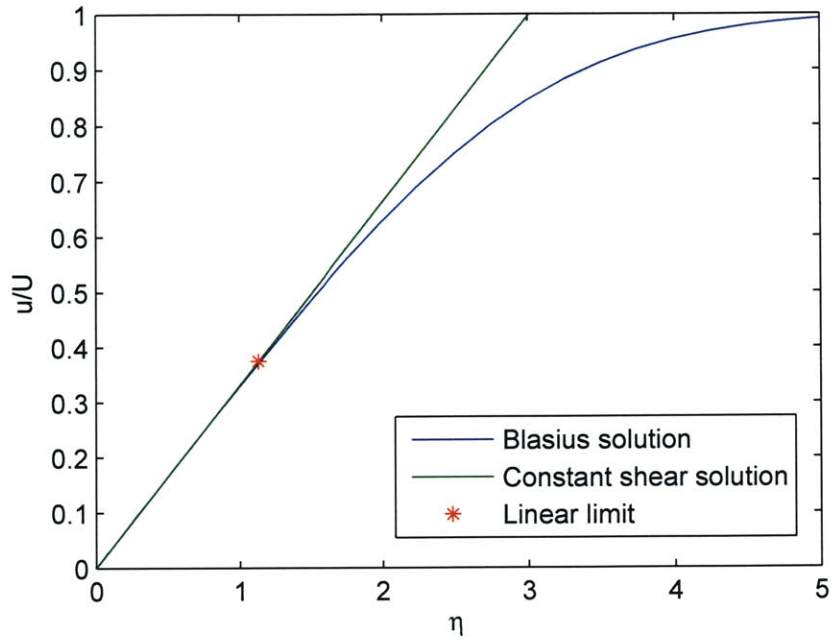

Figure 3-6: Linear limit of Blasius velocity profile

At each node point in the velocity profile, the mean and standard deviation of u are calculated from N processed PIV images. The points that fall within the linear limit are fitted with a weighted regression line to find the wall-shear stress according to the formula:

$$u = A + By \tag{3.5}$$

where B is the slope of the regression line. For N statistically independent samples, this coefficient and its standard deviation, σ_B, are given as:

$$B = \frac{\sum w \sum wy^2 - \sum wy \sum wu}{\sum w \sum wy^2 - (\sum wy)^2} \tag{3.6}$$

$$\sigma_B = \sqrt{\frac{\sum w}{\sum w \sum wy^2 - (\sum wy)^2}} \tag{3.7}$$

where the weighting factor, w_i is defined as:

$$w_i = \frac{N}{\sigma_{u_i}^2} \tag{3.8}$$

The wall shear value, $(\partial u/\partial y)|_w$, is identical to the slope of regression line, and so:

$$\left.\frac{\partial u}{\partial y}\right|_w = B = \frac{\sum w \sum wy^2 - \sum wy \sum wu}{\sum w \sum wy^2 - (\sum wy)^2} \tag{3.9}$$

$$\sigma_{\left.\frac{\partial u}{\partial y}\right|_w} = \sigma_B = \sqrt{\frac{\sum w}{\sum w \sum wy^2 - (\sum wy)^2}} \tag{3.10}$$

Chapter 4

Optical shear stress sensor evaluation – results

This chapter presents results of wall-shear calculated for a flat plate boundary layer using the experimental apparatus and methods described in chapter 3. For the sake of simplicity wall-shear was studied rather than the skin friction, though the two measurements are related by equation 2.2. In brief, wall-shear measured with a Measurement Science Enterprise MicroS Shear Stress Sensor was investigated and compared with wall-shear derived from PIV velocity profiles for a range of free stream velocities.

Seven free stream velocities (measured from the ensemble average of 120 PIV velocity profiles) were studied to evaluate the optical shear stress sensor. These velocities are presented in table 4.1.

Experiment number	Free stream velocity (m/s)
1	0.1035
2	0.1450
3	0.1939
4	0.2420
5	0.3095
6	0.3670
7	0.4439

Table 4.1: Free stream velocities studied

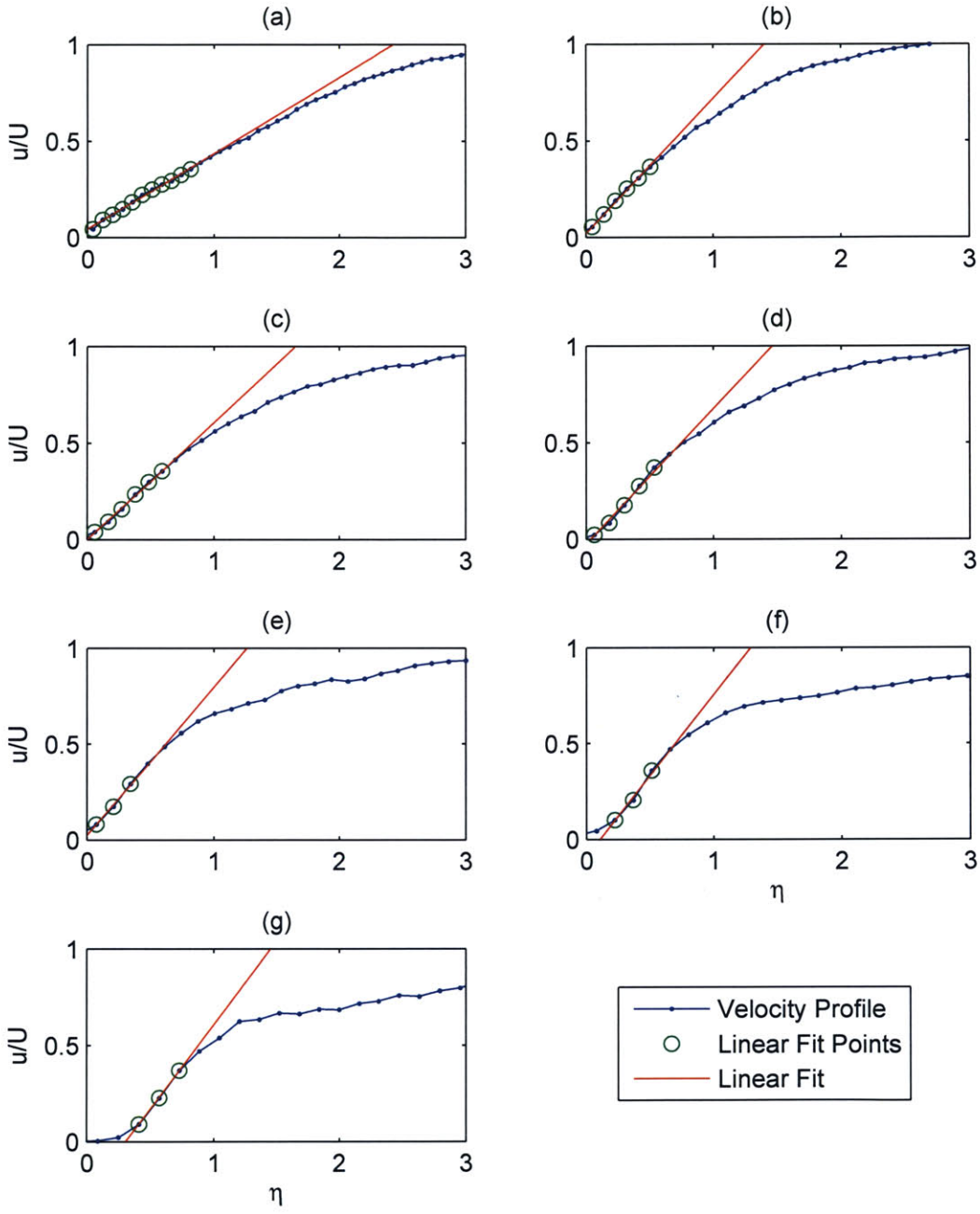

Figure 4-1: PIV velocity profiles and regression lines fitted to the linear region of the boundary layer for (a) 0.1035 m/s, (b) 0.1450 m/s, (c) 0.1939 m/s, (d) 0.2420 m/s, (e) 0.3095 m/s, (f) 0.3670 m/s, and (g) 0.4439 m/s

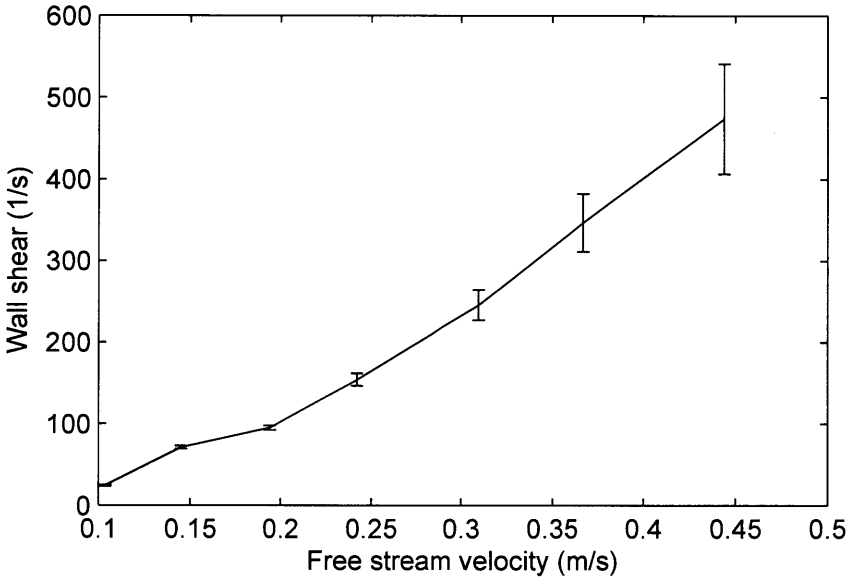

Figure 4-2: Wall shear derived from PIV velocity profiles for 120 images

4.1 Wall-shear from PIV

Mean PIV velocity profiles, resulting from the ensemble average of 120 images, were calculated at the sensor location for the seven free stream velocities studied, and linear curves were fitted to the linear region of the boundary layer in order to determine the wall-shear in each case. The results of the curve-fitting are given in figure 4-1, and show the PIV velocity profile, the fitted curve, and the points inside the linear region of the boundary layer used to create the regression line. It should be noted that the curve fitting algorithm did not constrain the fitted velocity curve to pass through the origin. Experimental error in determining the exact location of the wall in the PIV images was high due to reflections at the wall, and imposing a no-slip condition at the wall would introduce these errors into the calculation of the wall-shear. In addition, several of the larger free stream cases resulted in clearly incorrect velocity calculations very near the wall – this is evident in the first velocity vector in figure 4-1 (f), and the first two velocity vectors in figure 4-1 (g). These erroneous velocity points were not included in the wall-shear calculations.

The wall shear stress was derived from the slope of the linear regression lines in figure 4-1 using equation 3.9, and the results are plotted in figure 4-2. Errorbars

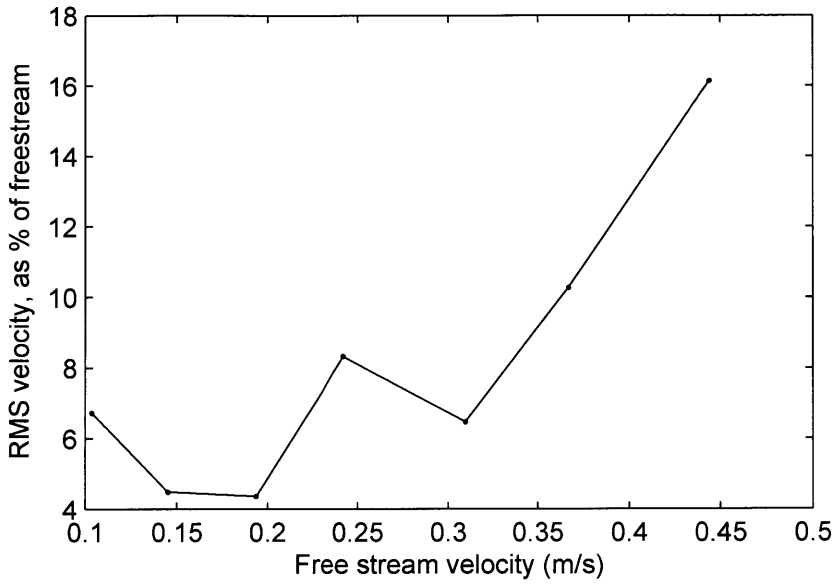

Figure 4-3: RMS velocity within linear region of the PIV velocity profiles for 120 images

in figure 4-2 correspond to the 95% confidence interval of the mean wall-shear at each point, where the confidence interval is based on the standard deviation of the mean wall-shear, given in equation 3.10. The wall-shear increases with free stream velocity, as expected. In addition, the error bars increase with free stream velocity as well. This can be attributed to two factors: first, the velocity fluctuations increase with increasing free stream velocity, which in turn decreases our confidence in the velocity vectors used for the linear fit. The velocity fluctuations can be seen from figure 4-3, which shows the average of the RMS velocity for all points within the linear region of the boundary layer. Second, the boundary layer gets thinner as the free stream velocity increases, and the number of velocity vectors calculated within the boundary layer decreases. The result is fewer points available for the linear fit, and a corresponding decrease in our confidence in the accuracy of the fit.

With the wall-shear from the PIV velocity profiles serving as the baseline measurement, wall-shear will now be measured with the optical shear stress sensor and compared with our baseline.

Free stream velocity (m/s)	Mean frequency (Hz)	High-pass cutoff (Hz)	Low-pass cutoff (Hz)
0.1035	520.09	100	2000
0.1450	988.05	200	5000
0.1939	1498.56	300	5000
0.2420	2433.71	500	10000
0.3095	5633.00	1000	15000
0.3670	8118.38	2000	15000
0.4439	10840.25	2000	20000

Table 4.2: Band-pass filter cutoff frequencies

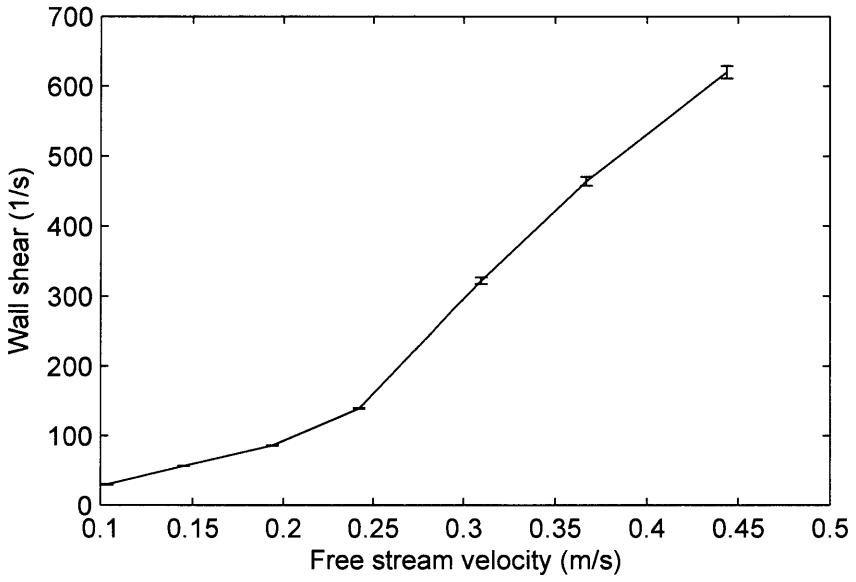

Figure 4-4: Wall shear from shear stress sensor

4.2 Wall-shear from optical shear stress sensor

The optical shear stress sensor was installed on the flat plate water channel model, as described in chapter 3, and 2000 samples were collected for each free stream velocity (the exception being the slowest case of 0.1035 m/s free stream velocity, where 562 samples were collected in 20 minutes before acquisition was halted). The high-pass and low-pass cutoff frequencies of the band-pass filter, given in table 4.2, were determined experimentally such that high and low frequency noise was eliminated, yet the desired signal was not attenuated. The minimum required signal-to-noise ratio (SNR) was set to 1 dB.

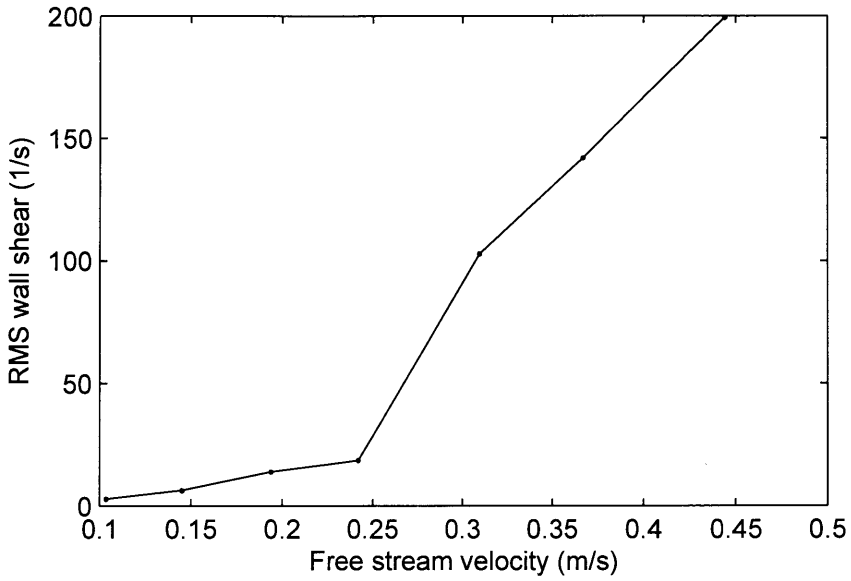

Figure 4-5: RMS wall shear from shear sensor

The mean wall-shear calculated from equation 3.1 for each free stream velocity is presented in figure 4-4. Error bars representing the 95% confidence interval are calculated based on the standard deviation of the mean wall-shear, which is given in equation 3.2. While the experimental scatter, plotted in figure 4-5 as the standard deviation of the wall-shear samples, became large relative to the mean wall-shear for the higher velocity cases, the number of collected samples resulted in a very high confidence in the mean wall-shear value, as evidenced by the small error bars. On the flip side, to achieve a high confidence in the mean wall-shear with this sensor, many samples must be collected, requiring large sampling times. The times required to collect 2000 samples ranged from greater than 20 minutes for the slowest free stream velocity (562 samples were collected in 20 minutes), to 63 seconds for the fastest free stream velocity.

Free stream velocity (m/s)	PIV wall-shear (1/s)	PIV st. dev. wall-shear (1/s)	Sensor wall-shear (1/s)	Sensor st. dev. wall-shear (1/s)
0.1035	24.08	0.46	29.75	0.12
0.145	71.15	0.98	56.52	0.14
0.1939	95.08	1.32	85.72	0.32
0.242	154.16	3.88	139.21	0.43
0.3095	245.70	9.52	322.21	2.34
0.367	346.70	18.09	464.37	3.25
0.4439	474.04	34.40	620.06	4.58

Table 4.3: Wall-shear from PIV and shear stress sensor

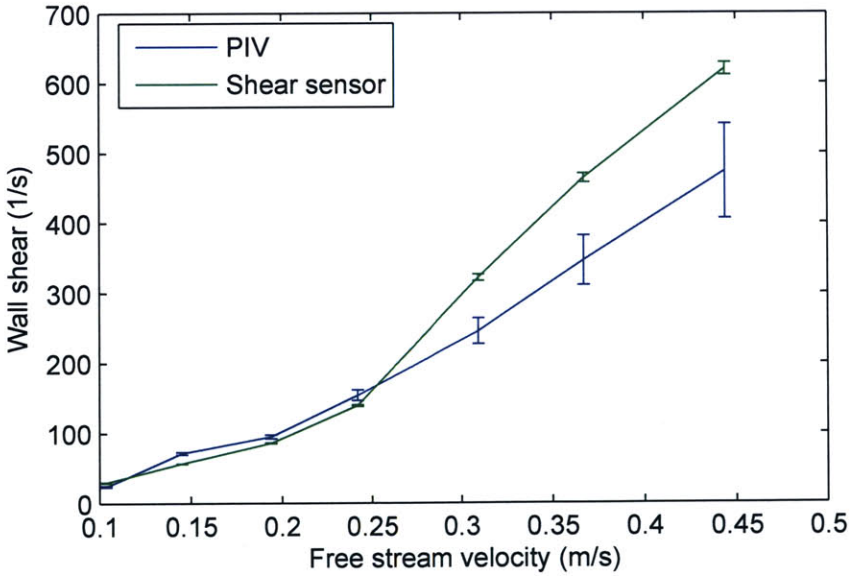

Figure 4-6: Wall shear from shear sensor compared to shear derived from PIV velocity profiles

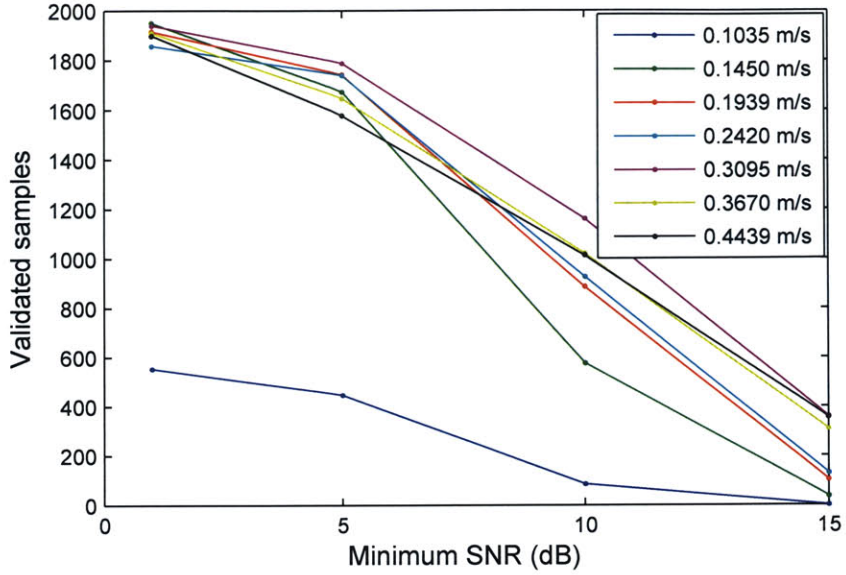

Figure 4-7: Number of validated samples with varying minimum signal-to-noise ratios, for several free stream velocities

4.3 Comparison between shear stress sensor and PIV

The wall-shear measured from the shear stress sensor was compared to that obtained from the PIV velocity profiles, and the result is tabulated in table 4.3 and shown in figure 4-6. While the wall-shear measurements from each technique follow the same trend, the measurements are statistically different to a 95% confidence level, based on the calculated error bars. The mean wall-shear measured with the shear stress sensor differed from the PIV-derived shear by between 10% and 34% over the range of free stream velocities studied. The difference in measurements prompted an investigation into the validation technique used by the shear sensor software to distinguish legitimate samples from signal noise. The findings are presented in the following section.

4.4 Signal-to-noise ratio and wall shear

The software supplied with the shear stress sensor includes a validation algorithm that rejects samples that do not exceed a minimum SNR threshold. Low-SNR samples may be caused by several phenomenon, including multiple particles passing through the laser fringe resulting in more than one signal frequency, or a particle scattering a very small amount of light resulting in a weak signal. The minimum SNR cutoff value determines how clean each sampled-signal must be to be considered a valid sample. By increasing the minimum SNR cutoff, a smaller percentage of samples is validated by the software. Figure 4-7 shows the number of validated samples from an identical set of data for increasingly strict minimum SNR cutoff values. 562 samples were collected for the 0.1035 m/s free stream velocity case, while 2000 samples were collected for all other free stream values. At first glance, it stands to reason that the samples validated with a stricter minimum SNR should provide a more reliable indicator of the wall-shear, and this hypothesis is examined below.

If each sample is plotted against its corresponding SNR value, the results shown in figure 4-8 are obtained. Note that the small cluster of low-frequency, low-SNR samples evident in figure 4-8 (f) and (g) are due to very large particles scattering light from more than one fringe at once, thereby creating a fundamental frequency smaller than the frequency corresponding to their actual velocity. These samples are typically filtered out with the band-pass filter, but in the cases mentioned, legitimate samples would be lost by further increasing the high-pass filter cutoff frequency.

It is clear from these figures that the mean wall-shear obtained from the shear stress sensor is not independent of the minimum SNR, but decreases with an increasing minimum SNR cutoff value. This is exhibited in figure 4-9, where the wall-shear curves measured with the shear stress sensor for varying minimum SNR cutoff values are again compared with the wall-shear derived from the PIV. The choice of the minimum SNR cutoff changes the measured wall-shear significantly. In fact, the wall-shear measured with the shear stress sensor can be made to match that obtained from the PIV much more exactly through the minimum SNR choice. The cause of

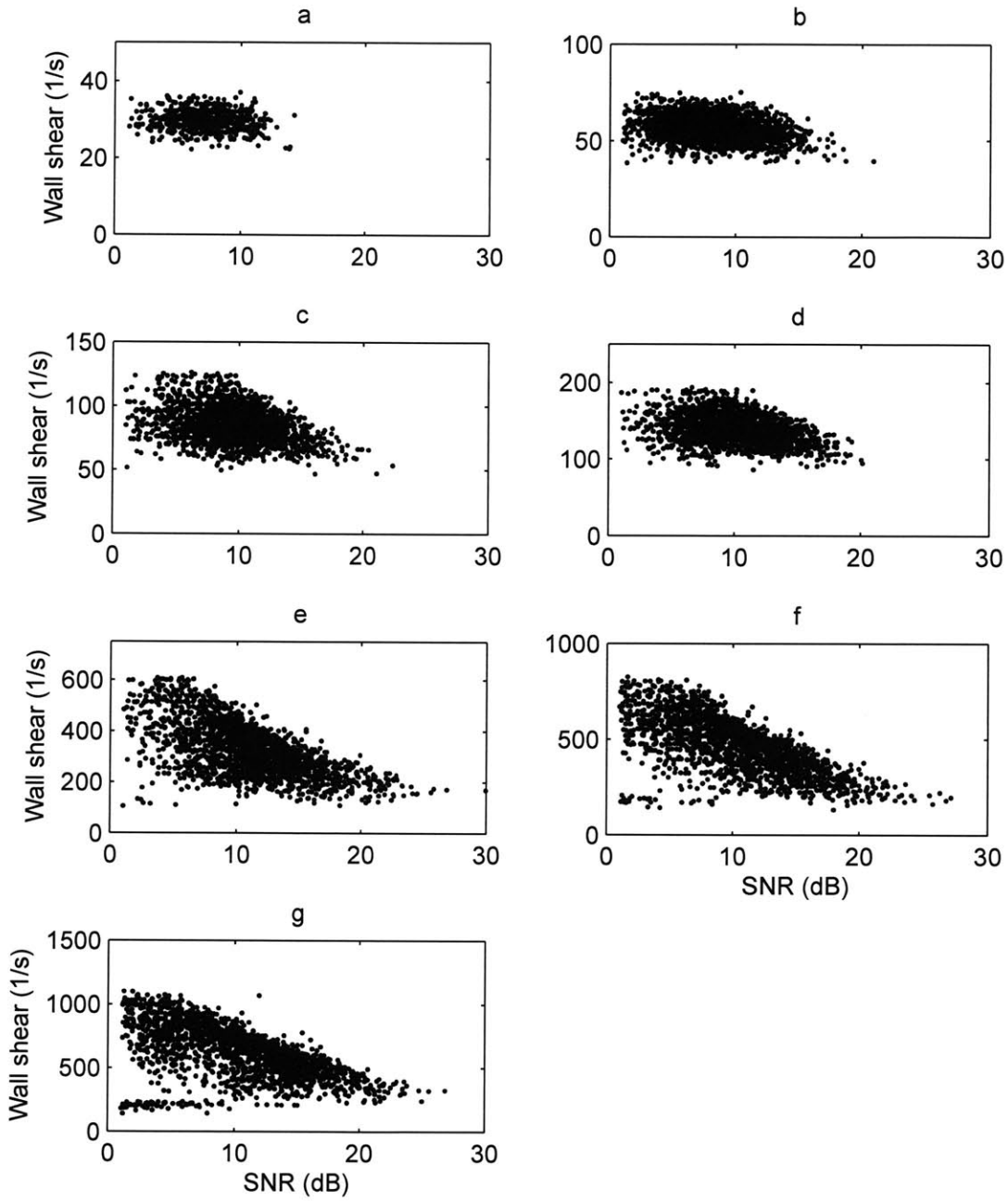

Figure 4-8: Plot of wall shear samples vs. signal-to-noise ratio (SNR) for (a) 0.1035 m/s, (b) 0.1450 m/s, (c) 0.1939 m/s, (d) 0.2420 m/s, (e) 0.3095 m/s, (f) 0.3670 m/s, and (g) 0.4439 m/s

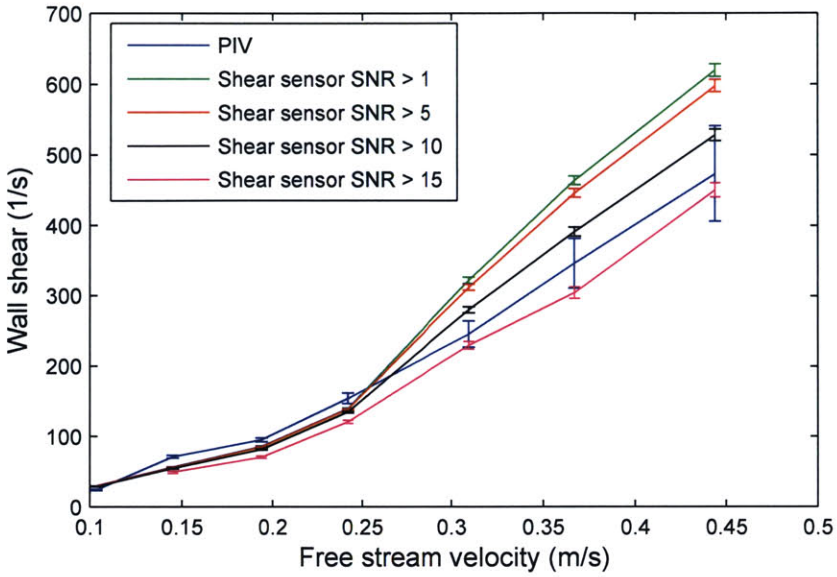

Figure 4-9: Wall shear with various minimum SNR cutoff values

the wall-shear dependence on the SNR needs to be investigated and corrected for accurate wall-shear measurements to be obtained with the shear stress sensor.

The wall-shear dependence on the SNR may possibly be attributed to several factors. First, it is apparent that for each free stream velocity, faster moving particles (which result in higher wall-shear measurements) tend to have a lower SNR while slower moving particles tend to have a higher SNR. This may be due to slower moving particles scattering more light than their faster counterparts, resulting in a stronger signal. However, as the free stream velocity is increased (resulting in an increase in the wall-shear, and an overall increase in the particle velocity), higher SNR samples are collected, suggesting that SNR cannot be attributed to particle velocity alone.

Higher SNR samples may also be due to the optical sensor receiving more scattered light from particles closer to the wall than those farther away. The sensor is designed to collect light from a measurement volume, and so particles from varying distances from the wall are sampled. The wall-shear calculated from each sample is designed to be independent of the distance from the wall, y, as shown in equation 2.5, so long as the sensor's measurement volume lies within the linear region of the boundary layer. Should the sensor be collecting samples from outside of the linear region, the

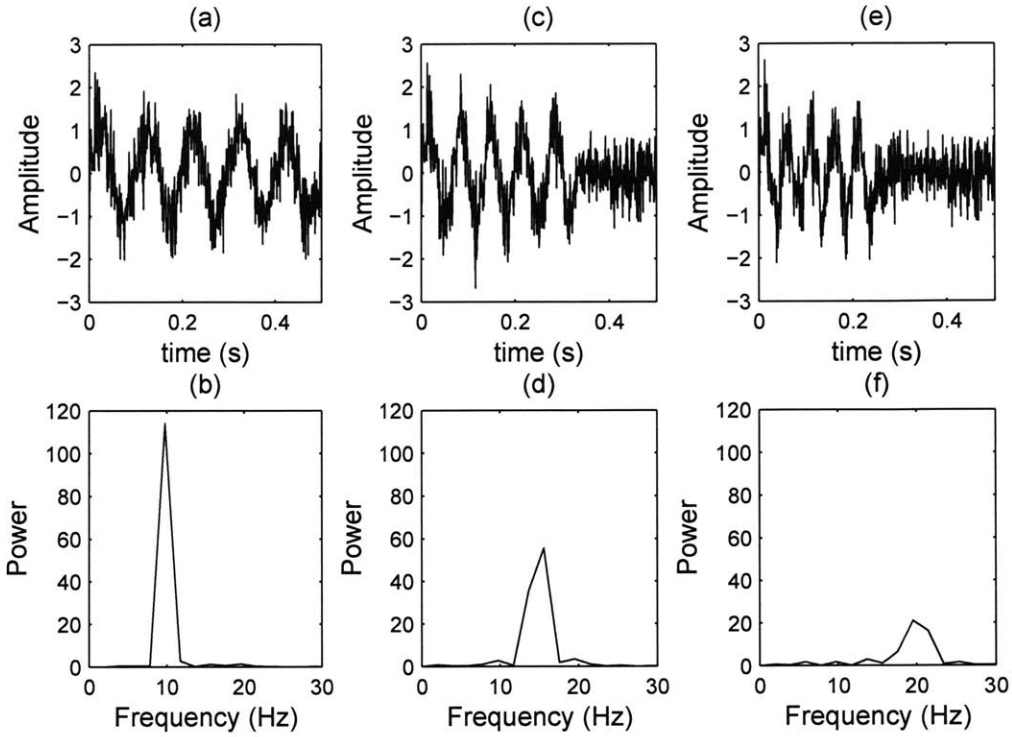

Figure 4-10: Power spectrum resulting from 5 periods of a sine wave corrupted with random noise for (a) & (b) a 10 Hz signal, (c) & (d) a 15 Hz signal, and (e) & (f) a 20 Hz signal. Identical random noise covered the entire width of the sampling window in all cases.

measured wall-shear may then become a function of the distance from the wall, and possibly the SNR as well. Given the relatively large boundary layer thickness of these experiments, however, it is unlikely that the measurement volume of the sensor lies outside of the linear region of the boundary layer.

A third option is that the calculated SNR of each sample is a function of the way that that sample was acquired. For instance, the band-pass filter may attenuate higher frequency (and higher wall-shear) samples more than lower frequency samples, resulting in artificially lowered SNR values for large wall-shear samples. In addition, the window length of each sample may impact the SNR. For each experiment, the length of the collected signal – the sampling window – is presumed constant, but the duration of the light scattered by each sample varies with the velocity of the particle (due to a fixed number of laser fringes). A slower particle would therefore provide

a signal that occupies a larger percentage of the sampling window, resulting in a larger SNR value. An example of such a situation is simulated in figure 4-10 by a sine wave superimposed with randomly generated noise. Five periods of a sine wave are simulated in figure 4-10 for: (a) & (b) a 10 Hz signal, (c) & (d) a 15 Hz signal, and (e) & (f) a 20 Hz signal. The higher frequencies (representing higher wall-shear samples) result in a significantly reduced ratio of signal amplitude to noise amplitude in the frequency domain. For the experimental data shown in figure 4-8 (g), sampled frequencies ranged from 2500 Hz to 19200 Hz, suggesting that a fixed window size may play a large role in determining the SNR of different frequency samples.

It is unclear as to which of the above options, or some other factor entirely, resulted in the SNR dependence seen in figure 4-8. However, it can not be assumed that high SNR samples provide a better estimate of the wall-shear. Further experiments specifically addressing these issues need to be performed.

4.5 Conclusions

As discussed in the previous section, wall-shear derived from the optical shear sensor for flows with small velocity fluctuations (relative to the free stream velocity) is similar to that derived from PIV velocity profiles. However, the difference between the two independent measurements cannot be attributed to random error, as evidenced by the experimental error bounds. Furthermore, in flows with high velocity fluctuations, an ambiguity exists as to the exact wall-shear measurement obtained from the shear sensor, due to a dependence of the calculated wall-shear on the SNR cutoff value. For the shear sensor to become a viable measurement technique in these types of flows, this problem needs to be addressed. It is recommended that users be given more control over the supplied sample validation and processing software, and that the validation procedure be made as transparent as possible.

In addition, while the shear stress sensor provides very high spatial resolution due to the small measurement volume, temporal resolution is tied directly to the sampling rate. In our experience, the sampling rate is quite slow in low-velocity flows, even

with very dense particle seeding. When experimental scatter is present in the data, many samples must be averaged to obtain an acceptable error bound on the mean wall-shear, and so time-dependent wall-shear measurements are not possible except over very large time scales.

Chapter 5

Separation in the rotor-oscillator flow – experimental methods

The goal of this portion of the thesis is to investigate the kinematic theory of unsteady separation for two-dimensional flow in an experimental setting. As such, an experimental arrangement was needed that would produce nominally two-dimensional flow, a separation point of large enough length and time scale to be readily observable, and a means of easily creating and manipulating flow unsteadiness. To the best of our knowledge, the simplest such flow that meets the above criteria is the rotor-oscillator flow. This flow was studied by Hackborn [4] both numerically and experimentally for Stokes flows. This chapter will discuss in detail our experimental apparatus and methods and our numerical simulations employed in this study, while chapter 6 will present our experimental findings.

To compute the separation location and profile in equation 1.3 and equation 1.4, a knowledge of the time history of the shear and pressure gradient at the wall is needed. Due to the inherent difficulty of directly measuring skin-friction and pressure gradients in a low-Reynolds number flow such as the rotor-oscillator arrangement, numerical simulations were used to determine these quantities. The numerical simulations were validated by direct comparison of streamlines and streaklines with the experimental data. The separation location and profile calculated using data from the numerical simulation were then compared with the experimental results.

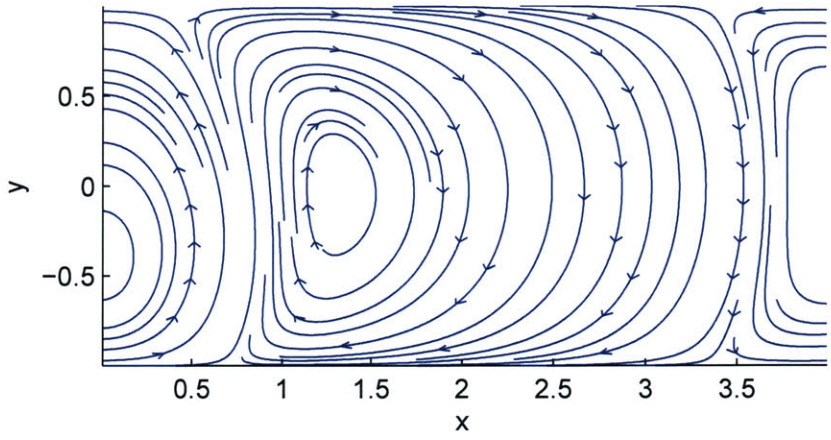

Figure 5-1: Rotor-oscillator flow streamlines in steady flow. The angular momentum source is located at $(x, y) = (0.0, -0.4)$

5.1 The rotor-oscillator flow

The rotor-oscillator flow consists of a point source of angular momentum in a two-dimensional flow between two parallel walls. Unsteadiness is introduced by oscillating the angular momentum source in a direction parallel to the walls. An example of streamlines resulting from the rotor-oscillator flow is given in figure 5-1. Separation and re-attachment points can be clearly seen along the upper and lower walls, with the separation point nearest the point source being the strongest separation point in the flow.

The rotor-oscillator flow is experimentally implemented by rotating a cylinder immersed in a rectangular tank, while simultaneously oscillating the cylinder in a direction parallel to the long walls. Figure 5-2 shows a schematic of this configuration. The strong separation point nearest the cylinder was chosen as the point to be studied in the experiments.

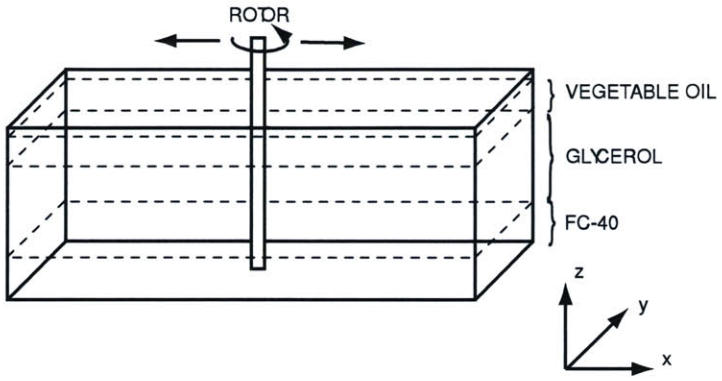

Figure 5-2: Sketch of the rotor-oscillator apparatus

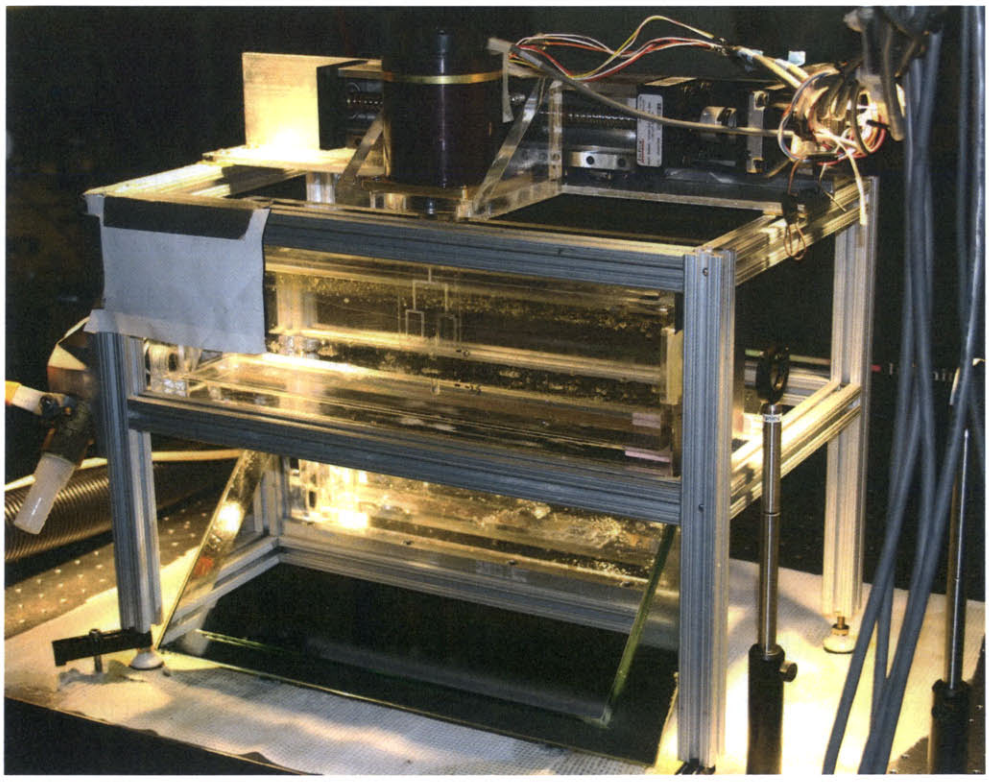

Figure 5-3: Rotor-oscillator apparatus

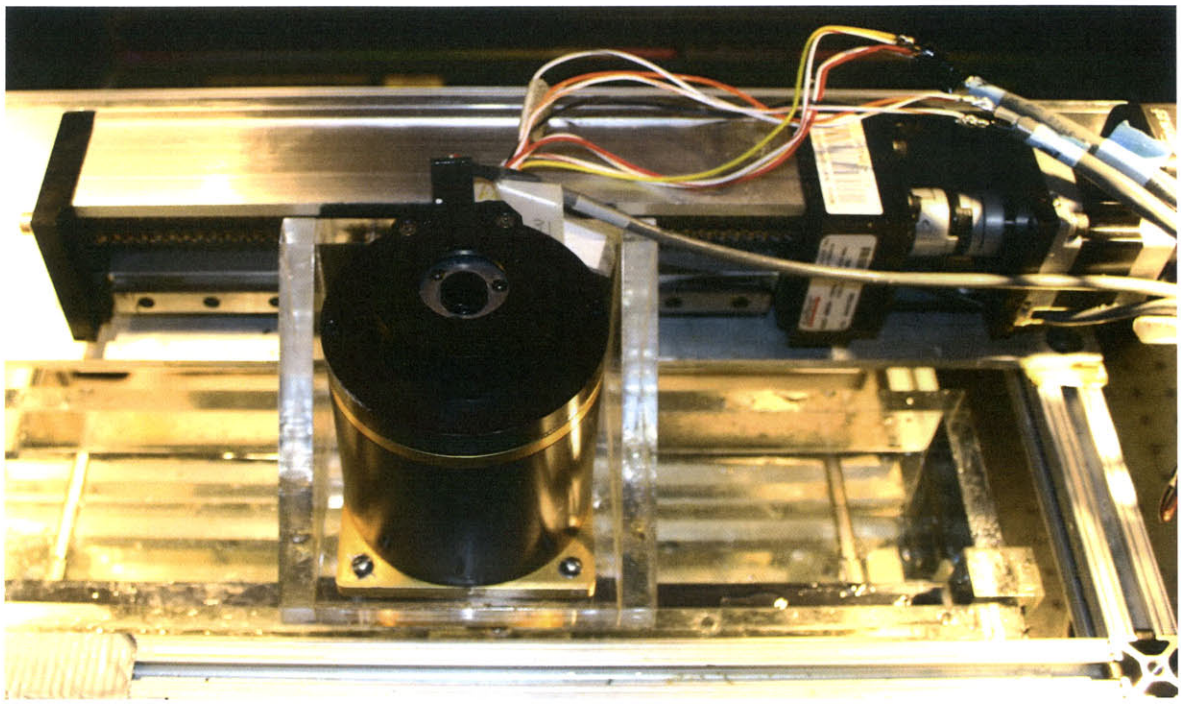

Figure 5-4: Rotation and translation control hardware

5.1.1 Rotor-oscillator experimental apparatus

A picture of the experimental rotor-oscillator apparatus is displayed in figure 5-3. The apparatus comprised an acrylic tank 40.2 cm long, 8.8 cm wide and 12.0 cm deep; with an open top, that stood in an elevated aluminum support frame with leveling mounts. The acrylic construction and elevated support frame provided for optical access to the fluid from all sides. An acrylic cylinder of diameter 6.39 mm was positioned vertically in the tank, at a distance of 26.20 ± 0.25 mm from the center of the cylinder to the 40.2 cm front wall. The cylinder was located midway between the 8.8 cm side walls, was fixed at the top to an inside-out type IOS34 stepper motor which provided rotation, and extended to within 1.0 cm of the bottom of the tank. The cylinder was aligned to be true, relative to the axis of rotation, to within 0.13 mm. The stepper motor was attached to a LINTECH horizontal translation stage aligned parallel with the front wall to within ± 0.25 mm at either end. The translation stage comprised a 1/4" lead screw, 10" in length, driven by an IOS stepper motor. Figure 5-4 shows the rotational stepper motor and translation stage. Both Rotation and translation of the cylinder

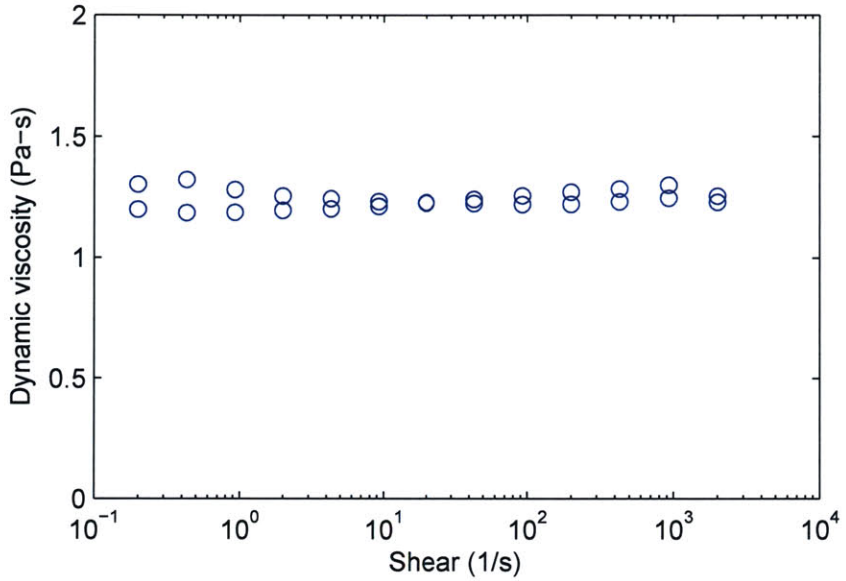

Figure 5-5: Dynamic viscosity of glycerol at 21 C

were controlled using a motion control system consisting of a National Instruments type PCI-7344 motion control card and National Instruments micro-stepping drivers.

A tri-layer fluid arrangement was set up in the tank, comprising a 2.8 mm thick bottom layer of FC-40 Fluorinert electronic coolant, a 5.0 mm thick center layer of glycerol (where the separation visualization took place), and a thin top layer of vegetable oil. The tri-layer arrangement was necessary to create 2D flow, as will be discussed in the following section. The fluid of interest, glycerol, has a density of 1262 kg/m^3 and a kinematic viscosity of 9×10^{-4} m^2/s. Glycerol was chosen due to its relatively high viscosity, resulting in a Reynolds number for the flow of order 1. In addition, glycerol was tested with a TA Instruments AR-G2 rheometer, and the dynamic viscosity was found to remain constant, such that the standard deviation of the dynamic viscosity was within 3.0% of the mean value over a wide range of shear values (figure 5-5). As such, glycerol can be taken to be approximately Newtonian.

In all experiments, the rotation of the cylinder was maintained at a constant rate of 20.89 rad/s (199.5 RPM), resulting in a Reynolds number for the flow, based on the tangential velocity of the cylinder due to rotation and the cylinder diameter, of 0.47. The cylinder was oscillated laterally with varying amplitudes and frequencies

for each experiment.

5.1.2 Obtaining two-dimensional flow

While the geometry of the rotor-oscillator arrangement nominally produces two-dimensional flow, in reality truly two-dimensional flow is much harder to create. End wall effects of the rotating cylinder and convection due to heating of the fluid and absorption of moisture from the air all resulted in three-dimensional flow. To mitigate these effects, several steps were taken. First, the cylinder end wall effects produced large three-dimensional structures. These structures were eliminated from the glycerol layer by adding a layer of FC-40 Fluorinert electronic coolant to the bottom of the tank. FC-40 was chosen due to its high density, 1900 kg/m^3, and low viscosity, 2×10^{-6} m^2/s, relative to glycerol. These unique properties resulted in the three dimensional effects of the end wall being contained in the bottom layer only. Second, the hydrophilic glycerol readily absorbs moisture from the air, resulting in convection currents. A thin layer of vegetable oil was added to the top of the tank to isolate the glycerol from the air. The final tri-layer fluid arrangement comprised a 2.8 cm thick bottom layer of FC-40, a 5.0 cm thick center layer of glycerol (where the separation visualization took place), and a thin top layer of vegetable oil. Finally, heat conducted from the stepper motor to the fluid, through the cylinder, drove convection currents in the glycerol. An acrylic cylinder was selected to eliminate this heat conduction and the associated three dimensional flow. The result of the previous steps is two-dimensional experimental flow, to the extent that over the course of a 10 minute experiment, no three-dimensional structures were detected with our visualization techniques.

5.1.3 Fluorescent dye visualization

Figure 5-6 shows a sketch of the apparatus set up for flow visualization. Separation was visualized by observing streaklines created by the laser-induced fluorescence of a neutrally buoyant dye mechanically injected through four injection ports in the

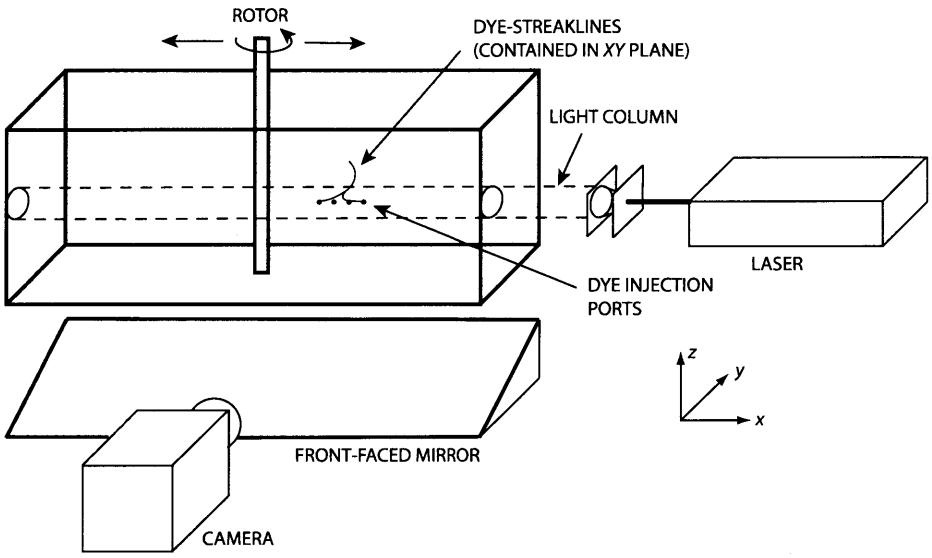

Figure 5-6: Sketch of the rotor-oscillator apparatus showing visualization method

sidewall boundary, at the mid-depth of the tank. The injection ports were 1.33 mm apart and had an exit diameter of 0.56 mm. The dye was supplied by a syringe pump at a rate of 1 ml/hour, and comprised a mixture of glycerol and fluorescein, for which the concentration of fluorescein was extremely small so as to not noticeably affect the density of the glycerol mixture. Motion of the dye was within a two-dimensional plane at the mid-depth of the tank. In each experiment care was taken to inject dye at points at least several millimeters away from the separation location so as not to affect the flow in the region of separation.

The evolution of the dyed-fluid in the horizontal plane was recorded using a CCD camera via a 45-degree front-faced mirror placed beneath the tank. The region of fluid near the wall was illuminated with a 490 nm wavelength laser light column to excite the fluorescein molecules. The camera lens was fitted with a 532 nm band pass filter which allowed only the light emitted by the excited fluorescent molecules to be recorded by the CCD camera. An example of experimental streaklines captured by this method is shown in figure 5-7. To account for parallax, the camera was calibrated by imaging a ruler that was placed in the horizontal plane of dye-injection prior to the start of the experiment. From this image, the correlation between pixels and millimeters was calculated, and this calibration factor was used to scale all sub-

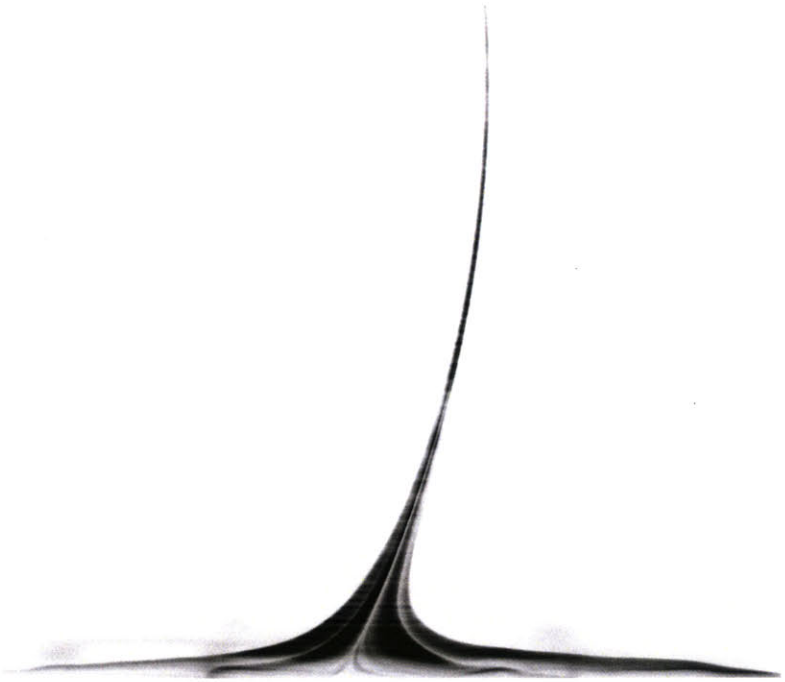

Figure 5-7: Dye streaklines observed from the laser-induced fluorescense of dye injected at the boundary

sequent images. Two types of CCD cameras were used to capture the images for the experiments. A Canon EOS-20D digital SLR camera was used in the case of steady flow, and in the period flow case to determine the separation location. However, due to the band pass filter attached to the lens, a long exposure time was needed to allow enough light to be captured by the CCD chip. To resolve the instantaneous separation location and angle in periodic and aperiodic flow, a more light sensitive LaVision Imager Pro X CCD camera was used, allowing a much shorter exposure time and higher frame rate. Moving to the Imager Pro camera, exposure times were reduced from 1.0 sec to 0.25 sec.

In unsteady flows, the start of the image acquisition process was triggered by the rotor-oscillator motion control model via a National Instruments data acquisition card. This method allowed each image to be timed precisely with the motion of the cylinder, which was then matched with a time step of the numerical simulation.

5.2 Numerical simulations

We computed the flow field numerically using Fluent's incompressible solver with a dynamic mesh. In the computations we use the cylinder as the point of reference rather than the tank reference, which results in the tank wall oscillating while the rotating cylinder is fixed. This allows us to use a fixed boundary-fitted mesh around the cylinder, while an orthogonal, dynamic mesh is placed near the straight-sided tank wall. The orthogonal dynamic mesh facilitates an easy and accurate computational implementation, and is computationally more efficient than the tank reference frame. In the cylinder reference frame a time-dependent source appears in the Navier-Stokes equations [2].

Skin-friction and pressure gradient profiles were extracted from the numerical flow field. The predictions for the separation location and the angle of separation were subsequently calculated from these numerical quantities, and compared with experimental results.

Chapter 6

Separation in the rotor-oscillator flow – results

This chapter presents the results of experiments on fixed separation in steady flow and periodic and quasi-periodic unsteady flows in the rotor-oscillator apparatus using the experimental setup and methods described in chapter 5.

6.1 Fixed separation

Fixed separation consists of a separation spike that originates from a single point on the boundary, either in steady or time-dependent flow. This occurs in any flow that results in a point on the boundary where the wall-shear averages to zero (equation 1.3). While the point of separation is fixed, however, the shape of the separation spike as it leaves the boundary may change in time.

The point of separation was determined in the images by observing the location of a very small (1-2 mm wide) dye-free region within the separation spike, near the wall boundary. This region contains the marginally-stable fixed point to which fluid particles are drawn, but never reach, before being ejected away from the wall. The specific estimate of the separation point within the empty region was found by observing the shape of the empty region as it leaves the boundary, and projecting this trajectory backwards to the wall. Figure 6-1 shows an example of the experimental separation

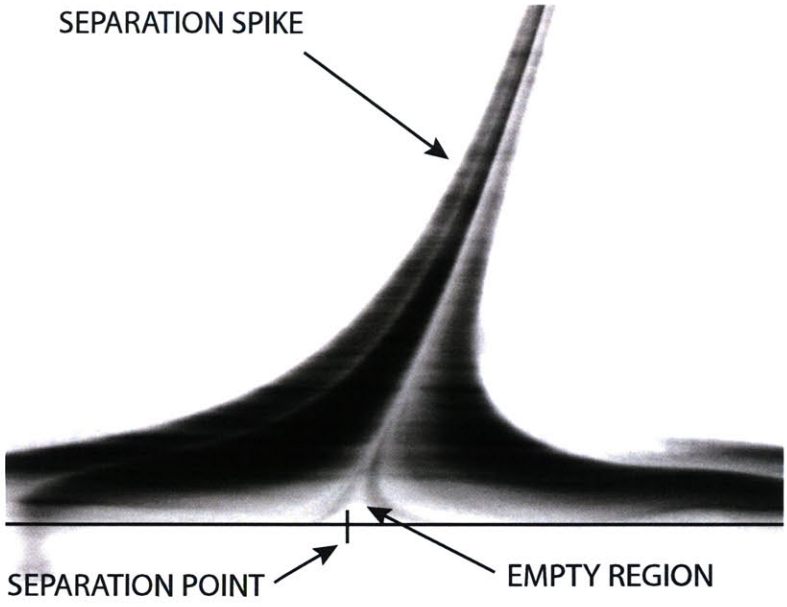

Figure 6-1: The experimentally determined separation point from dye streaklines

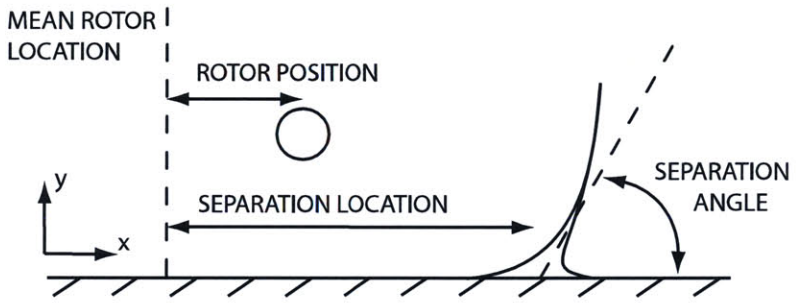

Figure 6-2: Experimental separation location and angle measurement conventions

point determined using the aforementioned approach. We define our experimental error to be the width of the dye-free region at the wall.

The separation location is measured relative to the mean rotor location, as shown in the sketch in figure 6-2. This point serves as a fixed reference point for the flow, and in unsteady flows the rotor position is also measured relative to this point. The separation angle is measured relative to the wall from the $+x$ direction.

6.1.1 Steady flow

To validate the experimental methods before moving to unsteady flows, the steady flow case resulting from no lateral oscillation was studied. The experimental separa-

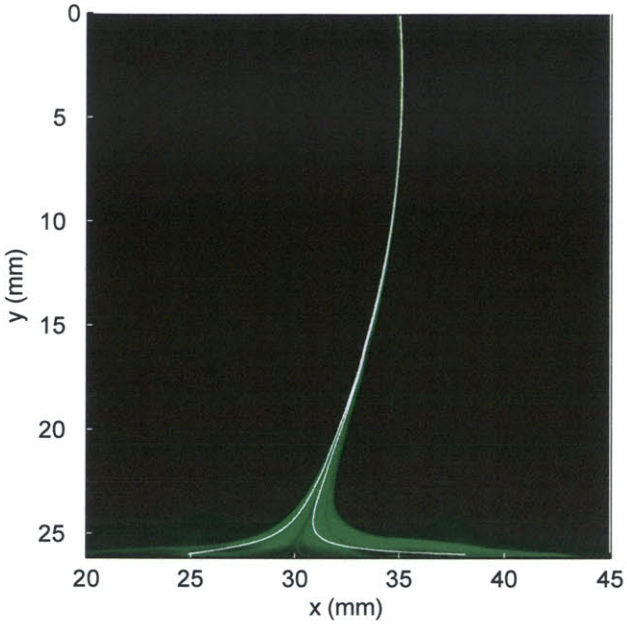

Figure 6-3: Separation spike in steady flow compared with numerically calculated streamlines (white lines)

tion profile was then compared with the well established formulae for the separation location and angle given by equation 1.1 and equation 1.2, calculated from data obtained in the numerical simulation.

Figure 6-3 shows the separation spike visualized from experimental streaklines. Superimposed are streamlines generated from the velocity field of the numerical simulation. In steady flow, the experimental streaklines follow the streamlines of the flow, and it can be seen that the location and shape of the experimental separation profile matches that of the numerical profile extremely well.

The predicted separation profile, to a linear approximation, is calculated from equation 1.1 and equation 1.2 and is superimposed on the experimental separation spike in figure 6-4. The location of the zero-skin-friction point falls well within the dye-free region in the experimental images, and the estimated separation location is 0.14 mm from that of the numerically determined separation point. The linear prediction of the separation angle also captures the near-wall geometry of the separation spike by lining up with the dye-free region, within the spike, that propagates away from

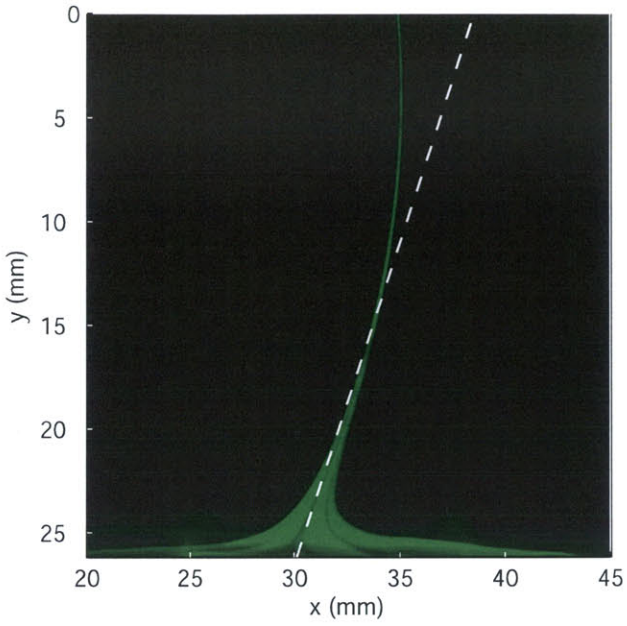

Figure 6-4: Separation spike in steady flow compared with linear separation prediction (dashed line)

the boundary.

Far from the wall the experimental separation spike deviates from the linear approximation of the predicted separation profile, as is to be expected given the wall-based approach. Higher-order terms, given in [3], can be included in the calculation of the separation profile; however, additional terms quickly lose accuracy as higher-order derivatives are required to calculate these terms. The quadratic term was calculated for the steady case, and the resulting equation was found to describe the separation profile:

$$y = 0.470x - 0.016x^2 \tag{6.1}$$

The quadratic coefficient is less than 4% of the linear coefficient for the steady case and, so long as x remains small, can be neglected for this flow.

Given the high level of agreement between experiment and numerics in the limit of steady flow, we now proceed with confidence to cases of fixed separation in time-dependent flows.

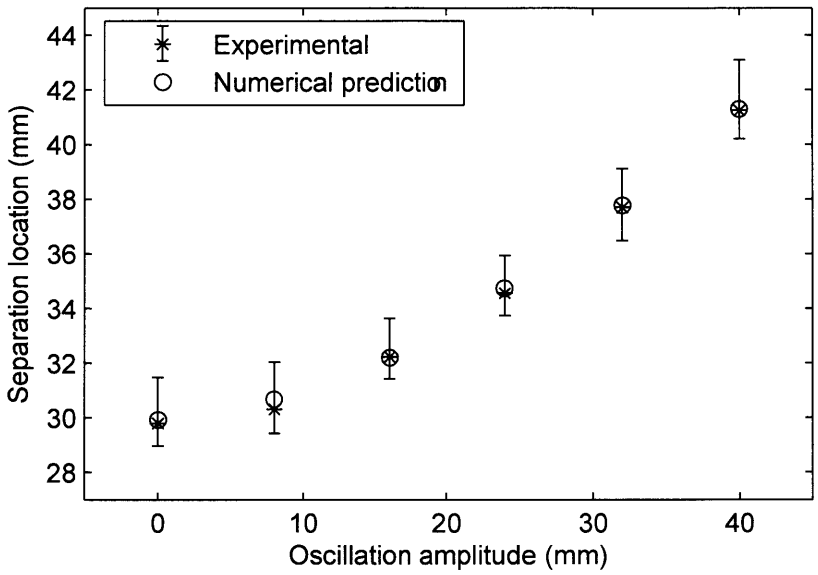

Figure 6-5: Experimental and predicted separation locations in periodic flows

Oscillation amplitude (mm)	Predicted separation (mm)	Experimental separation (mm)	Positive bound (mm)	Negative bound (mm)
0.00	29.93	29.80	1.68	0.83
8.00	30.67	30.31	1.72	0.88
16.00	32.19	32.23	1.40	0.80
24.00	34.74	34.57	1.37	0.83
32.00	37.78	37.69	1.42	1.22
40.00	41.30	41.24	1.85	1.03

Table 6.1: Experimental and predicted separation locations in periodic flows

6.1.2 Period flow

Periodic unsteady flows were generated by oscillating the cylinder laterally in addition to rotating it at a constant rate. The cylinder was oscillated with a sinusoidal motion, and with five different peak-to-peak amplitudes ranging from 8 mm to 40 mm, in 8 mm incremental steps. The period of oscillation was 6 seconds. In all cases, the separation location remained fixed over the entire period of oscillation, while the angle of the separation profile with respect to the wall varied.

The experimental separation point was compared with that predicted by the numerics using equation 1.5, and the results are shown in figure 6-5 for each amplitude

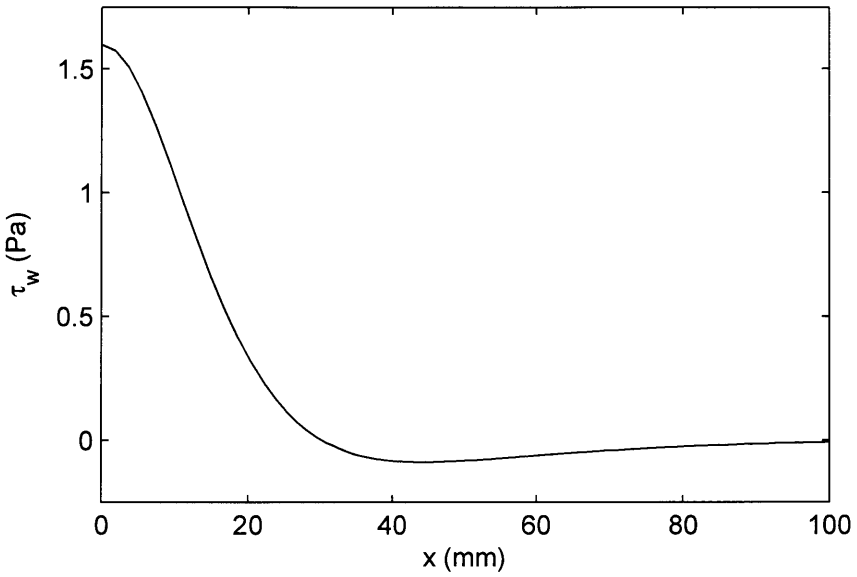

Figure 6-6: Wall shear stress profile in steady flow

studied, and also presented in table 6.1. The steady case is also included as 0 mm oscillation amplitude. In each case, the location of the time average of the zero skin-friction point fell within the error bars for the experimental separation location. We note that the bias in the error bars is due to the asymmetrical empty region caused by a large jump in flow velocity across the separation spike. The higher velocity particles to the left of the separation point are driven closer to the separation point before being ejected away from the wall relative to the slower velocity particles to the right of the separation point.

It can be seen that the amplitude of oscillation significantly affects the separation location relative to the mean rotor location. This can be understood by considering the skin-friction profile for the steady case, presented in figure 6-6. In a low Reynolds number flow such as this, oscillating the cylinder effectively oscillates the skin-friction profile (this is exact in the limit of Stokes flow). Due to the asymmetric skin-friction profile, when the cylinder is oscillated about its resting position, the average zero skin-friction point is 'pushed' more than it is 'pulled' by the rotor oscillation, resulting in a larger distance between the separation point and the mean location of the cylinder.

The orientation of the separation spike relative to the wall is calculated from

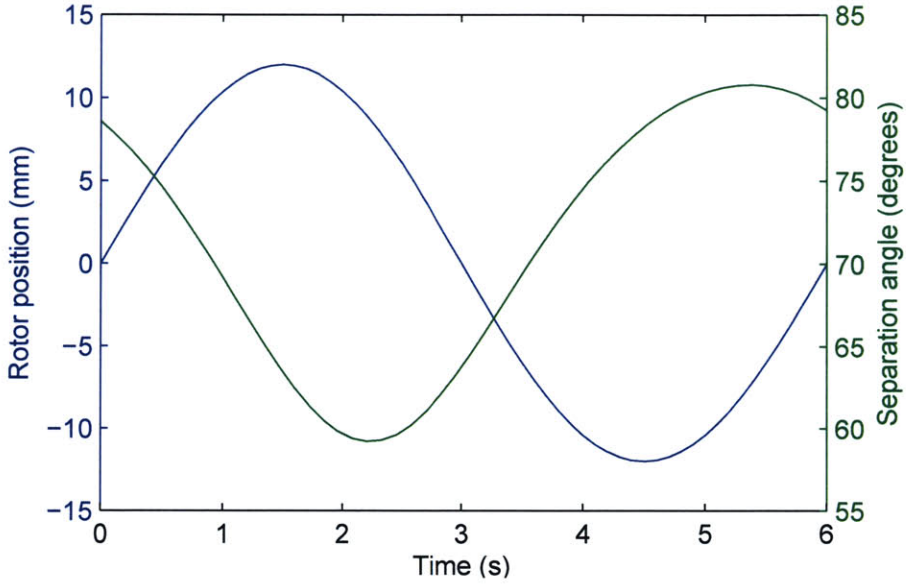

Figure 6-7: Numerical separation angle in periodic flow with a 24mm oscillation amplitude

the numerical data for the case of 24 mm oscillation amplitude with equation 1.6 and the results are shown in figure 6-7. The input sinusoidal motion of the cylinder produced a sinusoidal-like response in the separation angle, that was slightly more than 90 degrees out of phase. The separation angle, therefore, increased when the cylinder moved away from the separation point, and vice versa, with a small lag in the response.

The results from figure 6-7 were then compared with the experimental separation spike for the 24 mm amplitude case. The results are shown in figure 6-8 for three situations: the approximate minimum separation angle of 59.7 degrees (a), occurring 2.0 secs into the period of oscillation, the approximate mean separation angle of 71.3 degrees (b), occurring 3.7 secs into the period of oscillation, and the approximate maximum separation angle of 80.3 degrees (c), occurring 5.0 seconds into the period of oscillation. The predicted time-dependent linear profile falls within the experimental empty region containing the fixed separation point, and leaves the wall at the same angle as that of the experimental dye-free region to a very high accuracy for all three cases. Where the curvature of the experimental spike is small, such as figure 6-7(b) and (c), the linear numerical separation profile predicts the observed separation spike

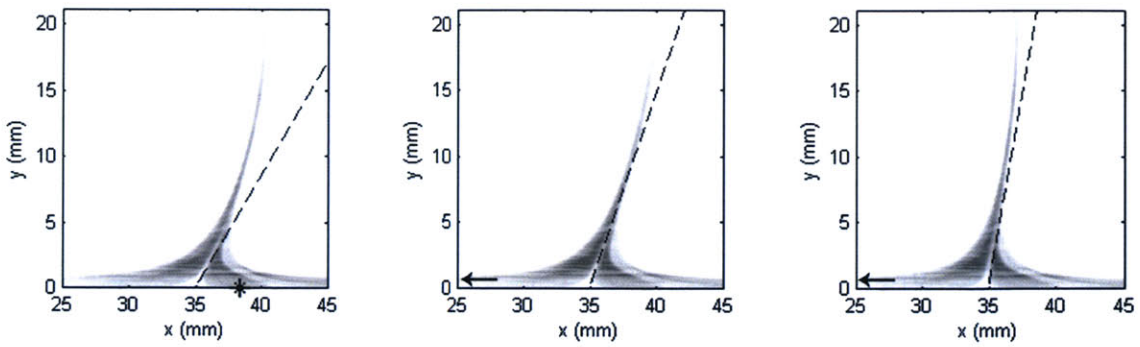

Figure 6-8: Separation spike in periodic flow (24mm oscillation amplitude) compared with the numerical prediction for (a) the minimum separation angle (t=2.0 sec) (b) the mean separation angle (t=3.7 sec) and (c) the maximum angle (t=5.0 sec). ($*$) or ($\leftarrow$) indicates the location of the instantaneous zero-skin-friction point.

for many millimeters away from the wall.

The instantaneous zero skin-friction point is also indicated in figure 6-8 as ($*$) for the exact location, or ($\leftarrow$) if it falls outside of the figure. As shown in figure 6-8, the zero skin-friction point does not, in general, mark the location of flow separation in a unsteady flow. While the zero skin-friction point does mark the location of the instantaneous separation streamline, the time scale of the oscillation of this zero skin-friction point is sufficiently large compared to the time scale of the fluid particle motion near the boundary that fluid particles cannot travel any significant distance along the instantaneous separation streamline. Instead, the fluid particles are ejected away from the boundary at a fixed separation point, as shown in figure 6-8.

6.1.3 Quasi-periodic flow

Quasi-periodic unsteady flows were generated by rotating the cylinder at 20.89 rad/s, while oscillating the cylinder laterally with a quasi-periodic motion. Each quasi-periodic signal – an example of which can be found in figure 6-9 – comprised a sum of twenty incommensurate frequencies and phase shifts. The frequencies and phase shifts which make up this signal are given in table 6.2, and were randomly chosen within a set range such that the physical limits of the experimental apparatus were not exceeded.

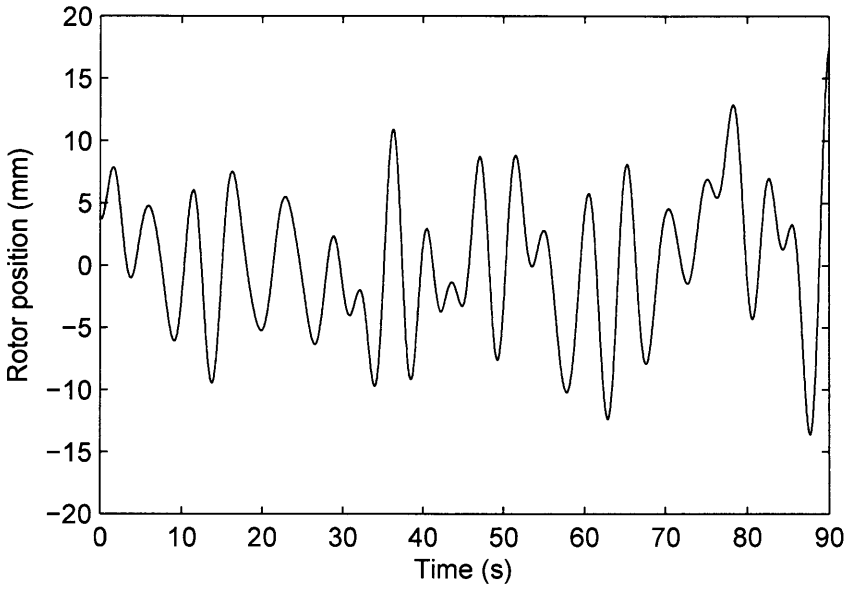

Figure 6-9: A quasi-periodic rotor signal having an RMS amplitude of 5.97 mm

Frequency (rad/s)	Phase shift
0.4056	0.6399
0.9542	1.3600
1.3038	-0.8544
0.8218	-1.0298
1.7707	-0.4533
0.0896	0.8022
1.6355	-0.6718
0.4591	1.3595
0.2394	1.3849
1.2828	1.0923
0.3825	-0.1411
0.1482	1.1031
1.0273	-0.5677
0.6852	1.1555
0.6802	-1.3393
0.3652	-1.4153
1.0358	-1.1878
0.9543	-1.2030
1.4072	-0.3925
1.5049	-1.4243

Table 6.2: Quasi-random signal frequencies and phase shifts

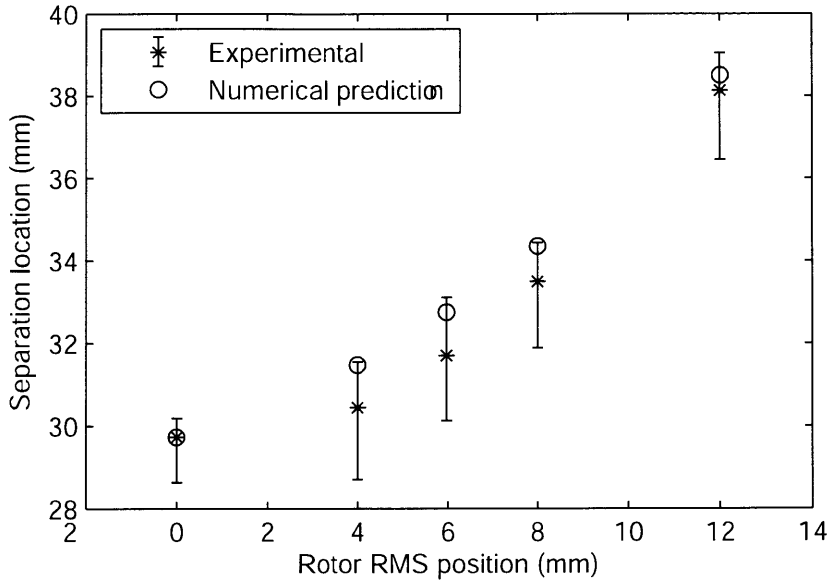

Figure 6-10: Experimental and predicted separation locations in quasi-periodic flows

RMS amplitude (mm)	Predicted separation (mm)	Experimental separation (mm)	Positive bound (mm)	Negative bound (mm)
0.00	29.73	29.74	1.10	0.46
4.00	31.47	30.45	1.74	1.11
5.97	32.75	31.70	1.57	1.41
8.00	34.35	33.49	1.61	0.94
12.00	38.50	38.13	1.69	0.92

Table 6.3: Experimental and predicted separation locations in quasi-periodic flows

A common amplitude was applied to each sinusoid in the signal, and this amplitude was scaled for different experiments to create motion of varying magnitudes. The oscillation magnitude was characterized by the signal RMS amplitude, and ranged from 4 mm to 12 mm.

The experimental separation point was compared with that predicted by the numerics using equation 1.3, and the results are shown in figure 6-10 for the range of signal RMS values, and also presented in table 6.3. The steady case is also included as 0 mm oscillation amplitude. In each case, the predicted separation location was larger than the experimentally determined location, but fell within the experimental error of the experiment. Error in the numerical separation location is present, however,

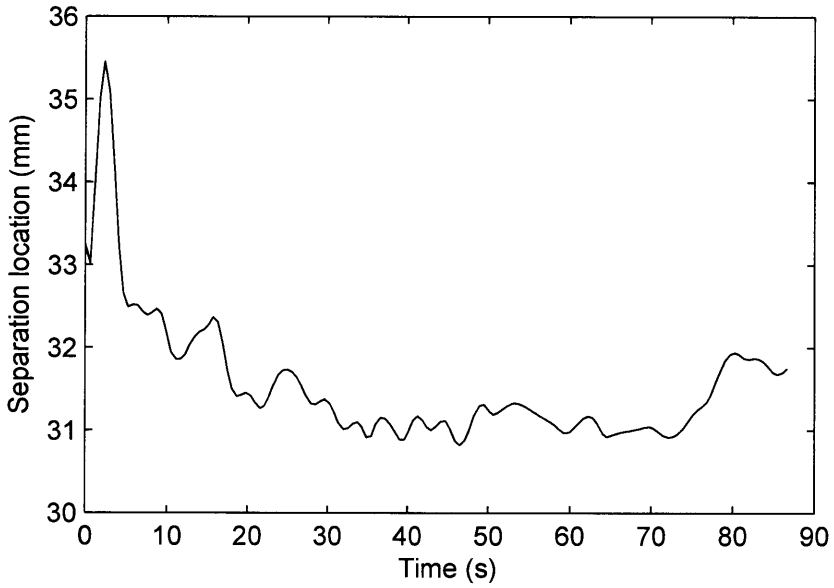

Figure 6-11: Convergence of the numerical separation in a 5.97 mm RMS quasi-periodic flow

due to the incomplete time history used to evaluate equation 1.3. The convergence of the numerical separation point to a fixed value can be seen in figure 6-11 for the 5.97 mm RMS case; it is evident that the separation point has not fully converged within the time span of the simulation and errors on the order of 1 mm can be expected.

The angle of the separation spike relative to the wall calculated from equation 1.4 is plotted over the length of the simulation time in figure 6-12 for the 5.97 mm RMS case. It should be noted that, in the case where equation 1.3 has not fully converged, equation 1.4 must be evaluated from measurements based on the effective separation location to obtain accurate results, where the effective separation location $\gamma_{eff}(t_0)$ is calculated from equation 1.3 over the time interval of $-\infty$ to t_0.

The separation angles from figure 6-12 were compared with the experimental separation spike at several time steps near the end of the simulation time span. The results are shown in figure 6-13, and cover three angles: an intermediate angle (a), occurring 52.3 secs into the simulation, a large angle (b), occurring 73.0 secs into the simulation, and a small angle (c), occurring 79.0 seconds into the simulation. While the exact separation point is over predicted by the numerics, as discussed above, the

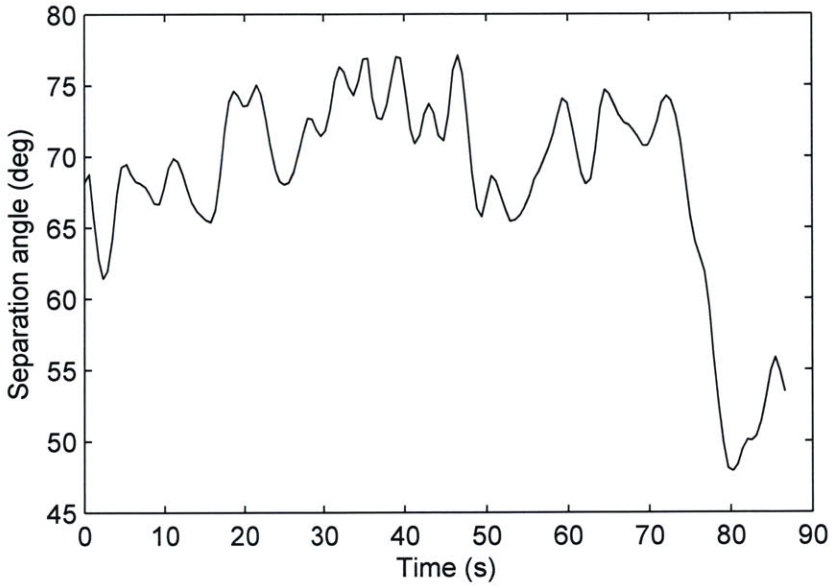

Figure 6-12: Separation angle in a 5.97 mm RMS quasi-periodic flow

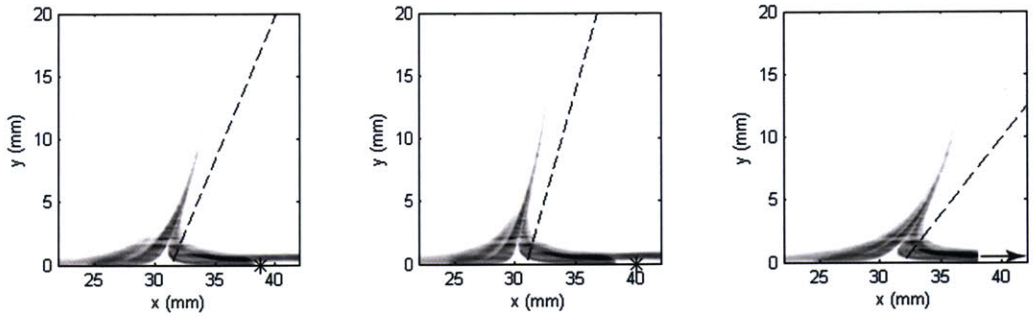

(a) (b) (c)

Figure 6-13: Separation spike in quasi-periodic flow compared with the numerical prediction for (a) an intermediate angle (t=52.3 sec) (b) a large angle (t=73.0 sec) and (c) a small angle (t=79.0 sec). ($*$) or ($\rightarrow$) indicates the location of the instantaneous zero skin-friction point.

angle of separation matches that of the experiments very well. It is also emphasized again that the instantaneous zero skin-friction point does not lie at the separation point in an unsteady flow, as demonstrated in figure 6-13.

6.2 Conclusions

The kinematic theory of separation has been shown to match experimental results to a high degree of accuracy for periodic unsteady flows. In the more general case, however, a time history approaching $-\infty$ is necessary for an exact solution. It was shown that for a finite window of flow data, in a quasi-periodic flow the kinematic theory again predicted the location and shape of the separation profile, but with larger errors than the periodic case. In particular, it was found that the convergence of the separation location to a fixed point required a relatively large time history. The predicted separation angle, however, matched the experiment after little time history.

Chapter 7

Conclusions

This thesis has investigated the kinematic theory of flow separation in an experimental setting for two-dimensional unsteady flows resulting in a fixed separation point. The goal of this research is to study the validity of the theory for tracking flow separation, as well as to examine aspects relating to the practical implementation the theory.

It was shown that for periodic, low Reynolds number flows, the kinematic theory of flow separation provides highly accurate predictions for both the separation location and angle of separation relative to the wall. These results, however, represent the ideal experimental test of the theory: the equations governing the location and shape of the separation location are exact in periodic flow, and the complementary numerical simulations provided high-accuracy, high-resolution measurements for the required flow properties.

Of more importance is how well the theory holds for general unsteady flows. It was found that for quasi-periodic, low Reynolds number flows, the theory predicted the separation angle very well, but resulted in small errors in the calculation of the separation location. These errors, stemming from the inability to provide flow measurements for a time history approaching $-\infty$, emphasize the importance of selecting a large enough time interval of data over which to implement the separation equations. A very large time interval ensures that the calculated effective separation location and profile approach the true separation location and profile, but a large time interval also incurs significant computational costs. Tracking separation in real time will require

the careful balancing of computational time versus accuracy.

The flows studied here were designed to result in a fixed separation point; however, tracking moving separation is also an unresolved problem, and one that needs to be addressed. Haller [3] has proposed a heuristic and a rigorous method for detecting moving separation, but this theory has yet to be investigated in an experimental setting.

A practical implementation of the unsteady separation equations studied in this thesis requires measurements of the pressure gradients and skin-friction profiles on the boundary to a high spatial and temporal resolution. Current technology provides few options for sensors that meet these requirements. A newly developed optical shear stress sensor was evaluated, with these needs in mind, due to its non-invasive measurement method, high sampling rate, and calibration-free design. An array of these sensors could be mounted on the surface of interest to provide the needed spatial resolution.

It was found, however, that the shear stress sensor had significant limitations for the low speed flows studied. Primarily, the dependence of the shear stress output on the input parameters (such as the minimum signal-to-noise ratio) must be resolved for the sensor to yield dependable results. Additionally, while the sensor is capable of achieving a very high sampling rate in theory, in practice high sampling rates could not be obtained in low speed flows. For high speed flows, such as the flow over an airplane wing, this may not be the case, but such flows were not tested here.

In summary, significant hurdles must be overcome to provide real time tracking of unsteady separation – be it fixed or moving. The kinematic theory of separation, evaluated here in a low Reynolds number, two dimensional flow, has not been tested at high Reynolds number or compressible flows common to aerodynamic applications. Moving separation has also not been experimentally studied in the context of the kinematic theory of separation. Additionally, it is necessary that the computational process of implementing this theory be optimized to allow real time processing. Finally, high accuracy pressure and wall-shear sensors are needed to provide the data required for a successful prediction of the separation location.

Bibliography

[1] FOURGUETTE, D., MODARRESS, D., WILSON, D., KOOCHESFAHANI, M., & GHARIB, M. 2003 An optical MEMS-based shear stress sensor for high Reynolds number applications.*41st Aerospace Sciences Meeting and Exhibit*, January 6-9, 2003, Reno, Nevada, AIA Paper 2003-742.

[2] FUMAGALLI, M. 2002 *A numerical investigation of particle motion and deposition on a cross oscillating cylinder.* MS Thesis, University of Illinois at Chicago, Chicago, IL.

[3] HALLER, G. 2004 Exact theory of unsteady separation for two-dimensional flows. *J. Fluid Mech.* **512**, pp. 257-311.

[4] HACKBORN, W. W., ULUCAKLI, M. E., & YUSTER, T. 1997 A theoretical and experimental study of hyperbolic and degenerate mixing regions in a chaotic Stokes flow. *J. Fluid Mech.* **346**, pp. 23-48.

[5] KUNDU, P. K. & COHEN, I. M. 2004 *Fluid Mechanics* 3rd ed. Elsevier Academic Press, Amsterdam.

[6] LIGHTHILL, M. J. 1963 Boundary Layer Theory In *Laminar Boundary Layers* (ed. L. Rosenhead). Dover.

[7] LIU, C. S. & WAN, Y.-H. 1985 A simple exact solution of the Prandtl boundary layer equations containing a point of separation. *Arch. Rat. Mech. Anal.* **89**, pp. 177-185.

[8] MOFFATT, H. K. 1964 Viscous and Resistive Eddies Near a Sharp Corner. *J. Fluid Mech.* **18**, pp. 1.

[9] PRANDTL, L. 1904 Über Flüssigkeitsbewegung bei sehr kleiner Reibung. *Verh. III, Int. Math. Kongr., Heidelberg* pp. 484-491.

[10] SEARS, W. R. & TELIONIS, D. P. 1975 Boundary-layer separation in unsteady flow. *SIAM J. Appl. Maths* **28** pp. 215-235.

[11] SHARIFF, K., PULLIAM, T. H., & OTTINO, J. M. 1991 A dynamical systems analysis of kinematics in the time-periodic wake of a circular cylinder. *Lect. Appl. Math.* **28**, pp. 613-646.

[12] VAN DOMMELEN, L. L. & SHEN, S. F. 1982 The genesis of separation. In *Numerical and Physical Aspects of Aerodynamics Flow* (ed. T. Cebici) pp. 283-311. Long Beach, California.

[13] YOUNG, A. D. & HORTON, H. P. 1966 Some results of investigation of separation bubbles. *AGARD CP* No. 4, pp. 779-811.

[14] YUSTER, T. & HACKBORN, W. W. 1997 On invariant manifolds attached to oscillating boundaries of Stokes flows. *Chaos* **7**, pp. 769-776.